Tectonic evolution of the Nootka fault zone and deformation of the shallow subducted Explorer plate in northern Cascadia as revealed by earthquake distributions and seismic tomography

Jesse Hutchinson[1], Honn Kao[2], Michael Riedel[3], Koichiro Obana[4], Kelin Wang[2], Shuichi Kodaira[4], Tsutomu Takahashi[4], and Yojiro Yamamoto[4]

[1]University of Canterbury
[2]Geological Survey of Canada
[3]GEOMAR Helmholtz Centre for Ocean Research Kiel
[4]Japan Agency for Marine-Earth Science and Technology

November 22, 2022

Abstract

At the northern Cascadia subduction zone, the subducting Explorer and Juan de Fuca plates interact across a transform deformation zone, known as the Nootka fault zone (NFZ). This study continues the Seafloor Earthquake Array Japan Canada Cascadia Experiment to a second phase (SeaJade II) consisting of nine months of recording of earthquakes using ocean-bottom and land-based seismometers. In addition to mapping the distribution of seismicity, including an M_W 6.4 earthquake and aftershocks along the previously unknown Nootka Sequence Fault, we also conducted seismic tomography that delineates the geometry of the shallow subducting Explorer plate (ExP). We derived hundreds of high-quality focal mechanism solutions from the SeaJade II data. The mechanisms manifest a complex regional tectonic state, with normal faulting of the ExP west of the NFZ, left-lateral strike-slip behaviour of the NFZ, and reverse faulting within the overriding plate above the subducting Juan de Fuca plate. Using data from the combined SeaJade I and II catalogs, we have performed double-difference hypocentre relocations and found seismicity lineations to the southeast of, and oriented 18° clockwise from, the subducted NFZ, which we interpret to represent less active small faults off the primary faults of the NFZ. These lineations are not optimally oriented for shear failure in the regional stress field, which we inferred from averaged focal mechanism solutions, and may represent paleo-configurations of the NFZ. Further, active faults interpreted from seismicity lineations within the subducted plate, including the Nootka Sequence Fault, may have originated as conjugate faults within the paleo-NFZ.

Hosted file

essoar.10508717.1.docx available at https://authorea.com/users/534906/articles/598611-tectonic-evolution-of-the-nootka-fault-zone-and-deformation-of-the-shallow-subducted-explorer-plate-in-northern-cascadia-as-revealed-by-earthquake-distributions-and-seismic-tomography

Tectonic evolution of the Nootka fault zone and deformation of the shallow subducted Explorer plate in northern Cascadia as revealed by earthquake distributions and seismic tomography

Jesse Hutchinson[1,5], Honn Kao[1,2], Michael Riedel[3], Koichiro Obana[4], Kelin Wang[1,2], Shuichi Kodaira[4], Tsutomu Takahashi[4], and Yojiro Yamamoto[4]

[1] School of Earth and Ocean Sciences, University of Victoria, Victoria, BC, V8P 5C2, Canada

[2] Pacific Geoscience Centre, Geological Survey of Canada, Natural Resources Canada, Sidney, BC, V8L 4B2, Canada

[3] GEOMAR Helmholtz-Centre for Ocean Research Kiel, Kiel, Germany

[4] Japan Agency for Marine-Earth Science and Technology (JAMSTEC), Yokohama, Japan

[5] Now at the Univeristy of Canterbury, New Zealand.

Corresponding Author: Jesse Hutchinson

Key points:

- Seismic tomography supports an NW-SE increase in the intensity of deformation of the Explorer slab.

- Focal mechanisms collectively indicate local variations in stress along the southern Explorer plate.

- Tectonic evolution of the Nootka fault zone inferred by newly mapped hypocentre lineations and orientations.

Abstract

At the northern Cascadia subduction zone, the subducting Explorer and Juan de Fuca plates interact across a transform deformation zone, known as the Nootka fault zone (NFZ). This study continues the Seafloor Earthquake Array Japan Canada Cascadia Experiment to a second phase (SeaJade II) consisting of nine months of recording of earthquakes using ocean-bottom and land-based seismometers. In addition to mapping the distribution of seismicity, including an M_W 6.4 earthquake and aftershocks along the previously unknown Nootka Sequence Fault, we also conducted seismic tomography that delineates the geometry of the shallow subducting Explorer plate (ExP). We derived hundreds of high-quality focal mechanism solutions from the SeaJade II data. The mechanisms manifest a complex regional tectonic state, with normal faulting of the ExP west of the NFZ, left-lateral strike-slip behaviour of the NFZ, and reverse faulting within the overriding plate above the subducting Juan de Fuca plate.

Using data from the combined SeaJade I and II catalogs, we have performed double-difference hypocentre relocations and found seismicity lineations to the southeast of, and oriented 18° clockwise from, the subducted NFZ, which we interpret to represent less active small faults off the primary faults of the NFZ. These lineations are not optimally oriented for shear failure in the regional stress field, which we inferred from averaged focal mechanism solutions, and may represent paleo-configurations of the NFZ. Further, active faults interpreted from seismicity lineations within the subducted plate, including the Nootka Sequence Fault, may have originated as conjugate faults within the paleo-NFZ.

Data & Software

Seismograms used in this study were collected as part of the Sea-Jade II (Seafloor Earthquake Array – Japan Canada Cascadia Experiment, Phase II) project (Hutchinson, 2021). Arrival data, relocated hypocentres, focal mechanisms, *P*-wave tomography, and *S*-wave tomography can be found in Supplemental Tables A1, A2, B1, C1, and C2, which can be accessed from the Open Science Foundation repository: https://osf.io/5q9fb/?view_only=f67fbfee2011466ab879e547adb982fb. Waveform data can be obtained from JAMSTEC upon request.

The Natural Resources Canada - Earthquakes Canada database was searched using http://www.earthquakescanada.nrcan.gc.ca/stndon/NEDB-BNDS/bulletin-en.php.

Some plots were made using the Generic Mapping Tools version 5.4.2 (http://gmt.soest.hawaii.edu/; Wessel and Smith 1998).

Global Multi-Resolution Topography (GMRT) was used to generate high resolution topography and bathymetry for GMT maps (Ryan et al., 2009).

Plain language summary

Earthquakes frequently occur off the west-coast of Vancouver Island, British Columbia. These earthquakes are related to the interaction between two tectonic plates, the Explorer and Juan de Fuca plates, in a region known as the Nootka fault zone. These tectonic plates are also subducting beneath North America. For this study, instruments were deployed to the ocean bottom to study earthquake signals in this region for nine months. The earthquake signals allow us to locate the origin of the earthquakes, while mapping the origins allows us to identify fault structures. By identifying these faults, we can infer how they developed by their size, orientation, and location. We also use the earthquake signals to determine properties of the interior structure of the earth. This imaging technique, known as seismic tomography, has allowed us to visualize the geometry of the shallow Explorer plate. By combining earthquake and seismic tomography interpretations, we provide a level of detail for this region not previously seen. Future earthquake and tsunami hazard predictions will benefit from our interpretations, and our analysis will also provide an excellent analogue for similar environments across the world.

Introduction

The Cascadia subduction zone (CSZ) is defined by the subduction of the Explorer (ExP), Juan de Fuca (JdF), and Gorda plates, formerly parts of the Farallon plate, beneath the western margin of the North America plate (NAm) from northern Vancouver Island to northern California (Atwater, 1970). The CSZ is capable of producing M_W 9+ earthquakes, the last of which occurred during 1700 AD (Satake, 2003; Atwater, 2005), but it is unusually quiescent at present. Recent research that involved the use of ocean-bottom seismometers (OBS) (Toomey et al., 2014; Wang and Tréhu, 2016), has focused primarily on studying the JdF. Few OBS experiments, however, have focused on the ExP.

The Seafloor Earthquake Array Japan Canada Cascadia Experiment (SeaJade) is designed to monitor the shallow Cascadia subduction interface and surface and subducted parts of the Juan de Fuca and Explorer plates, as well as the Nootka fault zone (NFZ) between them (Figure 1). Up to thirty-five OBS were deployed off the west coast of Vancouver Island, Canada in two phases in 2010 and 2014.

Data from the first deployment (SeaJade I) during July – September, 2010, allowed for the delineation of the NFZ through hypocentre distributions. The NFZ is bounded to the north and south by two mature primary faults that extend into the Moho and run NE-SW, between which lie several less well-developed secondary conjugate faults. SeaJade I also provided some insight into the depths to velocity-contrasting interfaces including the oceanic Moho within the subducting plate. It was found that the oceanic crust is approximately 7 km thick just seaward of the subduction front (Hutchinson et al., 2019).

The second deployment (SeaJade II) recorded data for nine months, beginning in January 2014. Several OBSs were placed further north of the NFZ than during SeaJade I. During the same time, land seismometers were deployed in the Nootka sound region along the west coast of Vancouver Island to accompany the OBS network (Figure 1).

One of the most important objectives of SeaJade II is to define the shallow geometry of the subducted JdF and ExP. Our previous analysis of the SeaJade II data focused primarily on an M_W 6.4 earthquake that occurred on 24 April 2014, during our recording period, and the associated aftershocks referred to as the Nootka Sequence (Hutchinson et al., 2020). From these results, we were able to delineate a fault within the subducted ExP. The hypocentre distribution of the Nootka Sequence has revealed that the subducting plate is bending downward to the northwest, nearly perpendicular to the direction of subduction. The results showed that the NFZ not only marks a change in subduction rate and direction, but it is also a transition from the more shallowly dipping subduction to the south, to the more steeply dipping subduction to the north. Substantial evidence has been provided for this change in plate geometry in the analysis of the hypocentre distribution and in the complexity of focal mechanisms (Hutchinson et al., 2020).

3

In this study, we enhance the imaging of the down-bending ExP toward the northwest with the addition of three-dimensional (3-D) seismic tomography. The new seismic tomography combines the complete data from both SeaJade I and II to maximize resolution and spatial coverage. The tomography maps regions of low velocities that closely follow the hypocentre distribution of the Nootka Sequence, clearly distinguishing the two downgoing oceanic plates.

Additionally, the detailed analysis of the combined data highlights hypocentre lineations previously unnoticed within the NFZ. These seismogenic structures may reflect the tectonic characteristics of the paleo-NFZ when shear deformation was shallower and more broadly distributed. From this distribution and the orientation of focal mechanism trends, we can infer the developmental history of the NFZ.

Methods and Data Analysis

We adopt the hypocentre distributions and focal mechanism solutions reported in our previous two studies (Hutchinson et al., 2019, 2020). For this study, we have expanded the number of relocated hypocentres to 3,918 by adding events from before and after the Nootka Sequence and increasing the number of A-ranked focal mechanism solutions to 1,089. The associated arrival and relocated event data are provided in Supplemental Tables A1 and A2, and the focal mechanism data are provided in Supplemental Table B1. We compute initial locations using the 1-D velocity model from Spence et al. (1985) and the GENLOC location package (Pavlis et al., 2004) from the Antelope software suite. For further details, our initial location procedure is documented in Hutchinson et al (2020). For the complete SeaJade II dataset, we calculate location uncertainty by bootstrapping 80% of the associated phases over 1000 iterations for each event. Upon the removal of outliers, we found the average 3-sigma values for the major and minor error ellipses to be 2.9 and 1.2, respectively, and the depth error to be 4.5 km.

We utilize the TomoDD method to better determine the distribution of hypocentres and 3-D seismic velocity model for our study area (Zhang and Thurber, 2006). TomoDD jointly determines double-difference hypocentre solutions and inverts for the 3-D distribution of seismic velocities. The double-difference relocations are determined by utilizing travel-time differences of seismic phases (P and/or S) and waveform cross-correlations (Waldhauser, 2001). These data allow for the relative relocation of events to one another. TomoDD also accounts for the absolute locations of hypocentres so that both the accuracy and precision of hypocentre locations are greatly improved.

We determine the 3-D velocity model for a 200-by-200 km area with 2.1 km spacing centred around 49.25° N, 127.75° W. The vertical nodes are spaced more closely, at 1 km intervals to a depth of 52 km below sea level with the exception of the shallowest node, which is placed 1.3 km above sea level. To

test for the sensitivity of the velocity model to node spacing, we also perform joint inversions with horizontal node spacings of 3, 4, or 5 km. We find that low- and high-velocity structures are comparable between the different spacings; however, with larger distances between nodes the velocity outputs are coarser with more pronounced velocity highs and lows.

We implement event data from the SeaJade I catalogue (Hutchinson, et al. 2019) for a more robust seismic tomography model. The initial 4,573 events were input with ~136,000 associated P- and S-phases. Of these events, 3,918 could be relocated. Double-difference relocations and joint determination of 3-D velocities and relocations were alternated between steps of iterations. In total, we perform 78 iterations to calculate the final 3-D P- and S-velocity models. Parameters used for these computations are provided in Supplement C, while the V_P and V_S data are provided in Supplemental Tables C1 and C2, respectively. We also calculate V_P/V_S ratios for each grid cell from the P- and S-velocities. We computed a mean V_P/V_S ratio of 1.75 ± 0.04. Because we observed nearly equal numbers of P- and S-phases, and both types of phases were well-picked, we decide that this is the best method for determining the V_P/V_S ratio, unlike cases with poorer S-wave datasets (Eberhart-Phillips, 1990; Wagner et al., 2005; Zhang and Thurber, 2006).

We quantitatively compare the location errors before and after applying TomoDD. We estimate hypocentral location errors before TomoDD by the bootstrapping method described above. With TomoDD, errors are most accurately determined by examining subsets of the entire dataset with singular-value decomposition (SVD). We select two representative subsets of events, based on different OBS coverage. The northern subset of 116 events is taken from the northwestern segment of the Nootka Sequence area described in Hutchinson et al. (2020). For this subset, the bootstrapping-determined 3-sigma values for the major, minor, and depth of the error ellipsoids are, on average, 3.17, 1.28 and 7.77 km, respectively. By comparison, the average errors for the X, Y, and depth axes of the error ellipsoids after TomoDD are 0.66, 0.67, and 1.22 km, respectively.

The southern subset consists of 120 events from the southeastern segment of the Nootka Sequence area where the OBS coverage is better. For this subset, we find significantly lower errors with average errors for the X, Y, and depth axes of the error ellipses of 0.10, 0.14, and 0.15 km, respectively. By comparison, the bootstrapping errors have average 3-sigma values for the major, minor, and depth of the error ellipses of 2.92, 1.22 and 3.41 km, respectively. Overall, TomoDD relocations have reduced the location error by up to an order of magnitude.

We derive focal mechanism solutions for the entire SeaJade II catalog (including those from Hutchinson et al. 2020) using the program HASH (Hardebeck and Shearer, 2002, 2003). We use relocated hypocentres and path-dependent velocity structures to calculate the azimuth and take-off angle for our calculations. To ensure high-quality results, we use the peak displacements of P- and S-phases

5

to calculate S/P amplitude ratios. Events with 8 or more clearly identifiable first-motions are selected for calculating focal mechanism solutions. We found a total of 1,448 solutions (Supplemental Table B1), of which 1,089 are considered A-ranked.

Results and Interpretations

We take the magnitude of completeness (M_C) by b-value stability method (Cao and Gao, 2002) for determining the Gutenberg-Richter (G-R) distribution of seismicity that occurred during the SeaJade II deployment in our study area prior to (24 April 2014) and after (1 June 2014) the Nootka Sequence (Figure 2). We consider events within the bounds of 48.75-49.5° N and 127.5-129° W, roughly the area containing the NFZ. Standard deviations for G-R parameters are determined via bootstrapping 1,000 samples per test. Prior to the Nootka Sequence, a- and b-values and M_C are 3.82 ± 0.17, 0.87 ± 0.08, and 1.62 ± 0.14, respectively. Following the Nootka Sequence, a- and b-values and the M_C are 3.82 ± 0.11, 0.79 ± 0.05, and 1.76 ± 0.07, respectively. These b-values are higher than what was calculated for the Nootka Sequence, which is 0.72 ± 0.09 (Hutchinson et al., 2020) but lower than the b-value of 1.07 ± 0.08 from SeaJade I (Hutchinson et al., 2019). The b-values indicate that the ratio of high-magnitude to low-magnitude events was higher than during the SeaJade I experiment, even prior to the Nootka Sequence. Such a trend was most pronounced during the Nootka Sequence due to the mainshock event. The b-value from after the Nootka Sequence, which is lower than the prior time period, indicates that the tectonic regime had not completely returned to what was observed from SeaJade I (b-value ~1.0).

Hypocentre Distribution

Relocated hypocentres are shown in Figure 1. Seaward of the subduction front, the majority of seismicity is concentrated within the NFZ, with some diffuse epicentres in the ExP and JdF. Landward of the subduction front, most seismicity is located within the Nootka Sequence, with another, smaller concentration of events east of the southeastern terminus of the Nootka Sequence.

As inferred from SeaJade I observations, the Nootka fault zone is comprised of many faults, identified as primary and secondary. These faults are represented by lineations of hypocentres, which can be seen in Figures 1 and 3. Approximate fault strike, dip, width, and length for faults are provided in Table 1.

Since SeaJade I, several previously undefined zones of seismicity have been observed. The Nootka Sequence fault, described in Hutchinson et al. (2020), is the most obvious of these features, extending over 55 km in length with a width in excess of 6 km.

Another seismicity lineation, located 25 km east of the southern Nootka Sequence fault, extends approximately 17 km in length along a more northerly

trend in comparison to the Nootka Sequence fault, labelled as the Eastern Lineation (Figure 1). This seismicity distribution ranges in depth from 5 to 24 km and coincides with several historical earthquakes, including M_W 6.4 and 6.3 oblique strike-slip events that occurred on 19 July 2004 and 9 September 2011, respectively (based on the National Earthquake Database compiled by Natural Resources Canada, http://earthquakescanada.nrcan.gc.ca, last accessed August 2021). The occurrence of such large events near the lineation implies that it is likely a fault that has consistently reactivated and can generate M_W 6+ earthquakes (Figure 1).

Approximately 10-12 km southeast of the southern primary fault of the NFZ is a less well-lineated feature, labelled as the Southeastern Lineation. It extends for nearly 15 km before encountering the subduction front (Figure 3). Earthquake hypocentres continue to follow the trend of this lineation northeast of the subduction front for at least another 20 km, but are less well-clustered. Because these earthquakes are confined to shallower depths (extending to the depth of ~16 km) than those delineating the northern and southern primary faults (extending to the depth of 20 km) of the NFZ, and are more broadly distributed, we consider the fault responsible for these events to be less mature.

Seismic Tomography

To test the resolution of our seismic tomography model, we have performed several checkerboard tests with cube sizes of 10, 8, 5, or 3 km. We calculate synthetic travel-times for each phase using the finite-difference scheme of Hole and Zelt (1995). Checkerboard squares are set to have alternating velocities of $\pm 5\%$ of 5 km/s. We find that the minimum resolvable scale is generally 5 km, although 3 km cubes can be resolved in areas with the greatest raypath densities. The results from the 10, 8, 5, and 3 km resolution tests are shown in Figure S1a, b, c, and d, respectively. It should be noted that the checkerboard test results are limited due strictly to calculation only with synthetic travel-times, while our final tomography model also utilizes waveform cross-correlations and therefore has better resolution than indicated by the checkerboard tests.

The derivative-weight sum (DWS) of the raypath density, as determined with TomoDD, also provides a method of determining the areas within the tomography model with the highest resolution. We calculate the base-10 logarithm for each DWS value and contour the results in Figure S1. We have found that these results are consistent with the checkerboard output and provide a valuable means for discussing areas with sufficient resolution.

The 3-D tomography indicates both low- and high-velocity anomalies, defined as regions in which P-velocities, calculated over 1-km depth slices, are lower or higher than the average background velocities by at least 2%. In Figure 4, depths of 8, 16, 24, and 32 km are selected in order to focus on the shallower oceanic crust and oceanic mantle seaward of the subduction front, and the deeper oceanic crust and oceanic mantle landward of the subduction front.

Further, V_P/V_S ratios, presented in Figure 5, can indicate differences in structure and rheology to further corroborate features observed from the *P*-velocity tomography.

Landward of the subduction front, where the Nootka Sequence occurred, a low-velocity anomaly is present at a shallow depth of ~8 km at approximately 49.5° N 127.3° W and extends toward the northwest at greater depths, apart from localized variations, such as at the depth of 16 km (Figure 4). A high-velocity anomaly is adjacent to the low-velocity anomaly to the southeast. We infer that the low-velocity anomaly represents the oceanic crust of the subducting ExP, and that the high-velocity anomaly is the oceanic mantle. At the depth of 16 km, the SeaJade I results show a continuous low-velocity anomaly within the NFZ (Hutchison et al., 2019), which is consistent with the results from the combined dataset of both SeaJade I and II (Figure 4). The better coverage and distribution of SeaJade II stations around the NFZ, as well as the greater number of earthquakes over a longer period of time, allow for a more accurate and detailed tomography model, compared to a model based just on SeaJade I data. The updated tomography results show that low-velocity anomalies within the southwestern NFZ and landward of the NFZ appear to be separated by a high-velocity anomaly over a distance of approximately 30 km. This high-velocity anomaly is particularly apparent at depths of 16 and 24 km (Figure 4). Detailed tomography maps from depths of 20 to 31 km, the presumed depth range of the oceanic Moho discussed in Hutchinson et al. (2019), are shown in Figure S2.

V_P/V_S ratios within the NFZ (~1.5, Figure 5) are compatible with what was observed for SeaJade I (Hutchinson et al., 2019) at a depth of 16 km. The expanded catalogue has allowed us to image the low V_P/V_S ratios to a depth of 32 km around 49.1° N, 128° W. This coordinate coincides with the location of E3 (Figure 3), which may delineate the most seismogenic and presumably mature secondary fault within the NFZ.

In general, high-velocities and high V_P/V_S ratios east of the NFZ, within the Juan de Fuca plate, are consistent with the SeaJade I results (Hutchinson et al., 2019). Within the Explorer plate immediately west of the NFZ, seismic velocities appear to be higher than average, and V_P/V_S appears to be slightly lower at the depths of 16 to 24 km (Figures 4 and 5).

Several velocity profiles illuminate a change in the subducting slab geometry, from northwest to southeast (Figure 6). Areas with lower raypath coverage are shown with translucent white overlays on the velocity profiles. To accompany these profiles, we show derivative-weight sum contours of raypath densities with percent velocity perturbations from the original 1-D model (Figure S3), which indicate areas with the best-resolved tomography. In regions where the Vp tomography results vary the most from the initial 1-D model, raypath densities are sufficiently high to indicate that the lateral variation of seismic velocity cannot be an artefact. Orange dashed lines in Figures 6 and S3 represent the oceanic Moho, which is interpreted from the general increase in depth of low-

8

velocities within the tomography model and the distribution of hypocentres. From Hutchinson et al. (2019), the estimated seismogenic thickness of the oceanic Moho was found to be ~5-7 km, with a high concentration of earthquakes distributed near the crust-mantle interface. The depth to the top of the oceanic crust, indicated with dashed white lines in Figures 6 and S3 is extrapolated from the hypocentre distributions from this study and Hutchinson et al. (2020) and the assumed crustal thickness of ~7 to 8 km as determined in Hutchinson et al. (2019).

The 7.5–8.0 km/s *P*-wave velocity contours mark the transition from crust to uppermost mantle, i.e., the Moho discontinuity (Kao et al., 2013). Within the oceanic plate seaward of the subduction front, the 7.5 and 8 km/s contours are nearly horizontal, parallel, and separated by a depth interval varying from ~2 km (Profile C-C') to ~7 km (Profile A-A'; Figure 6). This is indicative of a nearly uniform, near-horizontal geometry of the Moho discontinuity seaward of the subduction front separating the lower crust and uppermost mantle. To the southwestern extent of profiles A-A', B-B' and C-C' (~0-20 km), the depth difference between the 7.5 and 8 km/s contours becomes significantly enlarged. This difference may represent the high degree of fracturing and-or deep mineral alteration of the upper mantle within the NFZ, as proposed by Rohr et al. (2018) and Hutchinson et al. (2019).

Past the subduction front, the 7.5 and 8 km/s contours diverge significantly. For example, along the northwesternmost profile (A-A'), located within the ExP, the slab is most likely more steeply dipping, since the 8 km/s contour goes from a depth of ~18 km to the lower limit of the tomography model at a depth 40 km (Figure 6). The geometry of the slab in this region is not well determined from the tomography. However, we can estimate the dip of the subducting ExP as ~23° based on the distribution of hypocentres. Northeast of the intersection of profile D-D' with A-A', a lens of high-velocity material overlies lower-velocity materials at a depth of approximately 20 km.

Within the NFZ, the velocity structure becomes more complicated on the landward side of the subduction front (profile B-B', Figure 6). At 45-70 km along profile B-B', a significant low-velocity anomaly is present at a depth of approximately 25-33 km. This anomaly occurs beneath the subduction front, and it appears to continue (with less certainty) in profile A-A'. At present, we do not have an explanation for this feature. Continuing along profile B-B' at approximately 70 km, the 7.5 km/s contour within the overriding plate appears to be deeper toward the northeast with several localized small-scale velocity variations. Similarly, the 8 km/s contour occurs at a depth of ~25 km at a model distance of 80 km along profile B-B' (Figure 6). Together, they are compatible with a subducted oceanic slab dipping at ~17°.

Further southeast, within the JdF, the dip of the subucting slab appears to be even shallower, although it is difficult to estimate the dip of the slab without a more robust downdip hypocentre distribution. However, based on the V_p tomography (profile C-C'), the 8.0 km/s contour landward of the subduction

front between the distances of 65 and 85 km shows an estimated dip of 13–15°.

Across profile D-D' (Figure 6), seismic velocities vary drastically at depths below 15 km. Southeast of the intersection with profile B-B', V_P is generally higher than to the northwest. In particular, lenses of low-velocity materials (< 7.5 km/s) are located at approximately 30 and 50 km along profile D-D' at depths of ~30 km and 17 km, respectively.

Seaward of the subduction front, velocities within the NFZ are higher than the initial 1-D velocity model. At a depth of ~16 km, V_P generally exceeds 8 km/s (Figure 4). This indicates that the upper mantle is located shallower within the NFZ near the subduction front than in the ExP, where V_P is less than 8 km/s at the same depth. We interpret the depth to the Moho within the NFZ to be ~13 km, where velocities exceed 7.5 km/s. In comparison, the oceanic crust of the ExP appears thicker (Figure 6, profile A-A'), potentially extending to the depth of 15 km with a less well-defined Moho than along the NFZ and JdF tomography (profiles B-B' and C-C', respectively).

Focal Mechanism Patterns

Focal mechanisms from before, during, and after the Nootka Sequence are shown in Figure 7a–c, respectively. In particular, we focus on the normal mechanisms to the west of the NFZ, reverse mechanisms to the northeast of the Nootka Sequence fault, and strike-slip mechanisms along the primary and secondary faults of the NFZ.

To better visualize the seismotectonic characteristics of individual structures, we provide representative focal mechanism patterns for areas of interest in Table 2 and show them in Figure 7d. We use the FMC code adapted from Álvarez-Gómez (2019). Specifically, we first compute the Aki-Richards (Aki and Richards, 2002) moment tensor components from the strike, dip, and rake for focal mechanisms grouped by rupture type and geographic setting. From these components, we then average and calculate the P-, T-, and B-axes of spatially grouped events with similar rupture types from the entire study. Finally, we compute the corresponding strike, dip, and rake for representative focal mechanisms from the averaged P-, T-, and B-axis vectors.

The NFZ is dominated by strike-slip mechanisms both before and after the Nootka Sequence. At 49.25° N, 128° W, the approximate motion of the ExP relative to the JdF is 219.35° from north at a speed of 2.5 cm/yr according to Model B of Braunmiller and Nabelek (2002), resulting in pure strike-slip relative motion between the two plates. Their Model A has a slight oblique-extensional component with a direction of 243.12° at 2.3 cm/yr. By comparison, the average trend of the T-axes for the northwestern Nootka fault (NNF) and southeastern Nootka fault (SNF) are in directions of 248.7° and 241.7°, respectively, which are more comparable to Model A.

Normal-faulting mechanisms west of the NFZ, within the ExP at approximately

49.15° N, 128.5° W, have strikes aligned roughly north-south. The average trend of the T-axes for the normal mechanisms is 275.8° (or 95.8°). Similarly, T-axes of nearby strike-slip events have an average trend of 272.9° (or 92.9°). The orientation of the T-axes is counter-clockwise to the relative motion between the ExP and JdF. In a regional context, distributed deformation can lead to complex rupture sequences, with variations in stress direction and magnitude over short distances. The presence of normal-faulting mechanisms is understood to reflect such stress heterogeneities.

Reverse mechanisms located above the subduction interface to the NE of the subduction front at approximately 49.7° N, 127° W are consistent with margin-normal compression caused by the subducting plate across the plate interface. The trend of the average P-axes of these focal mechanisms (40.7°) more closely matches the motion of the ExP with respect to NAm (2.1 cm/yr in a direction of 42.2° [Braunmiller and Nabelek (2002)]) than that of JdF (3.8 cm/yr in a direction of 60.8°) with NUVEL-1A (DeMets et al., 1994).

Tectonic Implications and Discussion

Northwestward Bending and Deformation of the Shallow Subducted Explorer Plate

The hypocentre distribution of the Nootka Sequence demonstrates variation in the geometry of the shallow subducted ExP as described in Hutchinson et al. (2020). From our prior study, it is proposed that toward the northwest, along the Nootka Sequence fault, the depth to the oceanic Moho increases from ~22 to 35 km (Figure 6) over a distance of 25 km. The change in Moho depth indicates a significant bend in the ExP nearly perpendicular to the direction of subduction.

In this study, we observe lenses of lower-velocity materials with increases in depth from the southeast to the northwest along profile D-D' (Figure 6) from depths of ~15 km to greater than 30 km. This change in *P*-velocity is representative of the overall change in the geometry of the subducting slab. The presence of deep low-velocity materials support the distribution of hypocentres as indicators of northwestward bending of the shallow subducted ExP.

Bending and unbending in the subducting plate toward the northwest are the most likely processes to create fractures, resulting in low V_P, not unlike the observations made for the deep low-velocity anomalies within the Nootka fault zone discussed in Hutchinson et al. (2019). The presence of these large, low-velocity anomalies at ~30 km and ~70 km along profile D-D' and at depths of ~30 km and ~17 km, respectively, could be magnified as a result of this high degree of fracturing.

Past a distance of 80 km along profile A-A', a lens of high-velocity materials is sandwiched between lower-velocity materials. Presumably, this lens could

be mantle materials overlaying the subducted slab, either the upper mantle of the overriding plate or oceanic mantle emplaced by margin-parallel mantle flow around the slab's edge. Shear-wave splitting analysis has indicated margin-parallel mantle flow in this region (Mosher et al., 2014), but whether it is induced at the edge of the subducted ExP further north, or by a more local intraslab tear (Hutchinson et al., 2020), as has been attributed to the fragmenting Cocos plate (Stubailo, 2015), remains unknown.

Tectonic Evolution of the NFZ

Faults from outside of the NFZ may be representative of a time when shearing was more broadly distributed (Rohr et al., 2018). The decrease in the length from the Nootka Sequence (~60 km) to the lineations that delineate the modern secondary conjugate faults (~10 km) between the northwestern and southeastern primary faults, probably implies that the NFZ has matured by changing from a more broadly distributed shear zone to a concentrated zone with well-defined bounding faults. The Nootka Sequence fault itself has also presumably grown and matured with time, as hypocentres are located within the oceanic mantle, similar to the northern and southern primary faults (Hutchinson et al., 2020), and unlike the conjugate faults within the NFZ (Hutchinson et al., 2019).

A lineation southeast of the southern primary fault (Figures 1 and 3; Table 1) may have formed at a time when the NFZ was broader. This lineation appears rotated clockwise by approximately 11° relative to the current NNF and 25° relative to the SNF. Another lineation observed east of the Nootka Sequence (Figure 1; Table 1), landward of the subduction front, also appears rotated clockwise by approximately 17° relative to the average strike of the NFZ conjugate faults and the Nootka Sequence (156°). Davis and Riddihough (1982) have demonstrated that the Explorer Ridge migrated to the northwest with the isolation of the Winona Block from the Pacific plate from ~4 to 1 Ma. The current position of the Winona Block is represented by a basin to the northwest of the NFZ, while the Explorer ridge is located to the northwest of the NFZ, marking the northern terminus of the Explorer plate. As migration of the Explorer Ridge occurred, clockwise rotation of the Explorer Ridge and the ExP reduced the rate of margin normal subduction.

In Figure 8, we present an illustrated evolution of the NFZ based on the rotation of seismic lineations and plate reconstructions from previous authors (Davis and Riddihough, 1982; Riddihough, 1984; Braunmiller and Nábělek, 2002; Rohr et al., 2018), expanding on the recent proposals of Savard et al. (2020). We interpolate the velocity vectors for relative plate motions between the ExP and JdF plates from an ~ 3.5 Ma to Model A of the present configuration as proposed by Braunmiller and Nábělek (2002).

3.5 Ma

At 3.5 Ma, the ExP subducted much like the northern JdF at a rate of ~ 5 cm/yr nearly perpendicular to the subduction front (Riddihough, 1984) at an orientation 15-25° counterclockwise to what is presumed today (Braunmiller and Nábělek, 2002). The exact configuration of the subduction front at this time is unknown, so it is portrayed as a straight dashed red line (Figure 8a). The oceanic lithosphere of the easternmost ExP is ~1 Myr old. The early NFZ formed at ~4 Ma as a result of the partial capture of the Winona Block from the Pacific plate by NAm, and at 3.5 Ma it is portrayed as a broad deformation zone with many smaller immature faults. The boundaries of the NFZ, the paleo-northwestern Nootka fault (PNNF) and paleo-southeastern Nootka fault (PSNF), are based on the maximum distance between the northern terminus of the Nootka Sequence Fault (NSF) and the Southeastern Lineation as well as the location of several strike-slip events to the northwest of the current NFZ. We have inferred that the current northern primary fault, demarcated as the northwestern Nootka fault (NNF), may have initiated as a conjugate fault during this time along with the Eastern Lineation, based on their paleo-orientations.

2.5 Ma

Clockwise rotation of the Pacific plate and the Explorer Ridge relative to NAm has led to partial capture of the Pacific plate by NAm. This capturing initialized the formation of the Winona block, reducing the convergence rate of the ExP (Davis and Riddihough, 1982). Due to rotation of the ExP and continued rupturing and evolution of the NFZ, we speculate that the NSF began as a conjugate fault (Figure 8b). The NNF continues to mature and lengthen nearly parallel to the direction of subduction. Subduction of the Eastern Lineation begins shortly before 1.5 Ma.

Development of the most well-defined conjugate fault (E3, Figures 3 and 7) may have begun during this time. The more northerly orientation in comparison to the other conjugate faults indicates that it may have undergone some rotation, and its well-defined lineation is suggestive of an older, more mature fault.

1.5 Ma

Further rotation of the ExP to the current azimuth led to lengthening of the NNF to the southwest (Figure 8c). Maturation of the NFZ has led to the formation of the current SNF and lengthening of the NSF, bridging the distance between the NNF and SNF. The NNF has further lengthened. As plate motion was accommodated by the narrower NFZ, the PNNF and PSNF were abandoned as active boundaries of the NFZ. Subduction of the NSF began.

Further northwest, at ~1 Ma, the Winona block was isolated from the Pacific plate. The subduction front may more closely resemble the present-day configuration, but it is still portrayed with a dashed red line to account for uncertainty.

0 Ma

The azimuthal difference between the orientation of paleo-faults and that of currently active faults indicates an average of 18° clockwise rotation (Figure 8d). Since 3.5 Ma the NFZ has matured and narrowed. The current NNF and SNF extend well into the mantle, acting as potential conduits for hydration of mantle materials. Conjugate faults, particularly E3, have become well-developed between the NNF and SNF. Rupturing along paleo-faults continues to occur regularly, as they were first noted during SeaJade I by Hutchinson et al. (2019), but much less frequently than the current actively developing faults.

Focal Mechanisms and Regional Tectonics

Section 3.3 and Table 2 discuss focal mechanisms in the area surrounding the NFZ in relation to current regional tectonic models. The orientations of focal mechanisms from the NNF and SNF generally agree with the sense of motion between the JdF and ExP. Focal mechanism solutions orient well with the associated faults (Figure 7d) and indicate left-lateral motion for the primary faults and right-lateral motion for the secondary conjugate faults. Low V_P and V_P/V_S ratios within the NFZ verify the results from SeaJade I (Hutchinson et al., 2019) and lend further support to the extreme fracturing and altering of the lower oceanic crust and upper mantle proposed by Rohr et al. (2018).

Outside of the NFZ, plate motion vectors inadequately explain the more northerly orientation reverse mechanisms northeast of the NSF. Because the averaged P-axes of the reverse mechanisms are nearly identical to the sense of motion between the NAm and ExP (Figure 7d), we propose that the northern JdF is subducting nearly 20° counterclockwise to the relative plate motions as determined with the NUVEL-1A model (DeMets et al., 1994). Brothers et al. (2020) calculated a new Euler rotation pole for the interaction between the Pacific plate and the NAm by analysis of morphological features and reconstructions of fault offsets along the Queen Charlotte fault. They proposed that relative motions between the two plates result in almost purely strike-slip behaviour, rather than having an oblique component (DeMets and Merkouriev, 2016). If so, this demonstrates that relative plate motions for both the JdF (DeMets et al., 1994, 2010) and ExP (Braunmiller and Nábělek, 2002) may require re-evaluation, as they both depend on the interaction between the Pacific and NAm plates.

An abundance of normal mechanisms within the ExP to the west of the NFZ indicates a locally dominant tensional stress field. Given the contrast between subduction of the southern ExP and the various interpretations of the Winona block: no subduction (Riddihough et al., 1980; Clowes et al., 1981), subduction (Davis and Riddihough, 1982), or transpression (Rohr et al., 2010), it is likely that the ExP is not acting as a single contiguous plate. Or alternatively, it could be in the process of reconfiguration. The normal mechanisms appear to line up with the strike of the Juan de Fuca Ridge when following its trace from

the south (Figure 7d). These mechanisms can be explained by regional shearing, where the T-axes align with 3.

Our observed focal mechanism solutions, deformation of the shallow subducted ExP, and the continuous evolution of the NFZ as determined from the distribution of faults (Rohr et al., 2018) and lineations of hypocentres (Hutchinson et al., 2019) are indicative of an unstable and changing tectonic regime. We propose that direct observations of the ExP and JdF in northern Cascadia, such as with seafloor geodesy, is required for re-evaluation of relative plate motions. Further seismic network surveys north of the SeaJade I and II OBS sites could provide a more accurate assessment of the internal deformation of the fragmenting ExP.

Conclusions

Three-dimensional seismic tomography in combination with our previous analysis of the hypocentre distribution of the Nootka Sequence (Hutchinson et al., 2020) confirms the downward bend in the ExP toward the northwest with plunging low-velocity structures representing the subducting plate. The estimated dip of the subducted plate just landward of the subduction front changes from 23° in the northwest to 13° in the southeast. Seaward of the subduction front, we estimate the depths to the oceanic mantle to differ between the JdF and ExP at depth of 13 and 15 km, respectively. Low V_P/V_S ratios within the NFZ extend to depths of ~30 km, particularly near the secondary fault E3, likely indicating high degrees of fracturing and localized shear deformation.

Averaged focal mechanism solutions represent localized stress orientations. To the southwest and west of the NFZ, roughly N-S strike oriented normal focal mechanisms provide evidence for a localized tensional stress field. Focal mechanisms within the NFZ confirm that it is controlled by strike-slip failure, aligning with the faults mapped by hypocentre distributions. Downdip of the subduction front, paleo-faults, such as the Nootka Sequence Fault and the Eastern Lineation (Figure 7d), exhibit complex rupture, presumably due to competing tectonic forces in the deformation of the ExP. Finally, thrust mechanisms within the overriding NAm are likely produced as a product of convergence, while the average P-axes (~40°) better align with the plate motion vector of the ExP than JdF relative to NAm.

The hypocentre distributions and focal mechanism solutions indicate currently active faults within the NFZ and the orientations of local stresses. Lineations of hypocentres located further from the primary and secondary faults of the NFZ have orientations rotated at an average of 18° clockwise, with more broadly distributed seismicity. We interpret these lineations as paleo-faults that were more active in the past but much less at present. These faults may represent the residual signature of a broader, less mature NFZ that began formation nearly 4 Ma with the capture of the Winona block (Davis and Riddihough, 1982).

Our observations provide direct evidence for extreme deformation of the ExP

15

and indicate that current plate rotation models (DeMets et al., 1994, 2010; Braunmiller and Nábělek, 2002) may not accurately capture the plate motions downdip of the subduction front. Further questions remain, such as how fragmented the ExP is, and where the limit of subduction is to the northwest. Addressing these questions in addition to our findings will lend to accurate seismic hazard prediction models for the northernmost extent of the Cascadia subduction zone.

Acknowledgements

Figure 1. Map of the study area of SeaJade II and the Nootka fault zone. The inset shows regional geography with the map area outlined using a red box. In this figure and all amp view figures of the is paper, earthquakes relocated with the double-difference method (Waldhauser, 2001; Zhang and Thurber, 2006) from this study are shown as circles with colour indicating depth. Historical earthquakes with magnitudes >= 4 are shown as colour-filled stars (Earthquakes Canada). Historic large magnitude earthquakes from 2004, 2011, and 2014 are labelled and shown as hexagons. Shape sizes are indicative of earthquake magnitude. Stations from both the ocean-bottom and land components of SeaJade II are shown as black triangles. The subduction front of the Cascadia subduction zone is indicated by the curving red line running from northwest to southeast with triangular teeth pointing in the direction of subduction (Gao, 2016). The location of the Winona block is from Gao et al. (2017) and Sypus (2019). The thinner red lines are 5 km contours of the plate interface based on the interpretation of Audet et al. (2010), with dashed contours representing highly uncertain

17

interface depths. Several areas important to discussion are circled with dashed
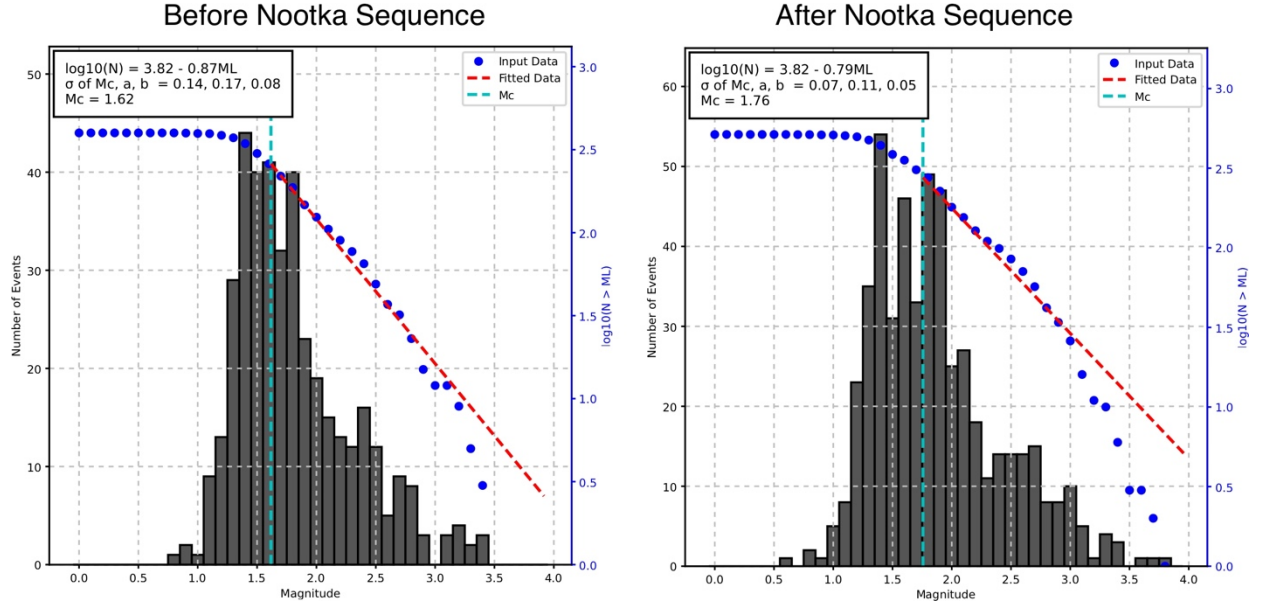black lines and labelled.

Figure 2. Gutenberg-Richter distributions of earthquakes within the Nootka
fault zone. (left) before the Nootka Sequence and (right) after the Nootka
Sequence. The M_C by *b*-value stability method (Cao and Gao, 2002) was used
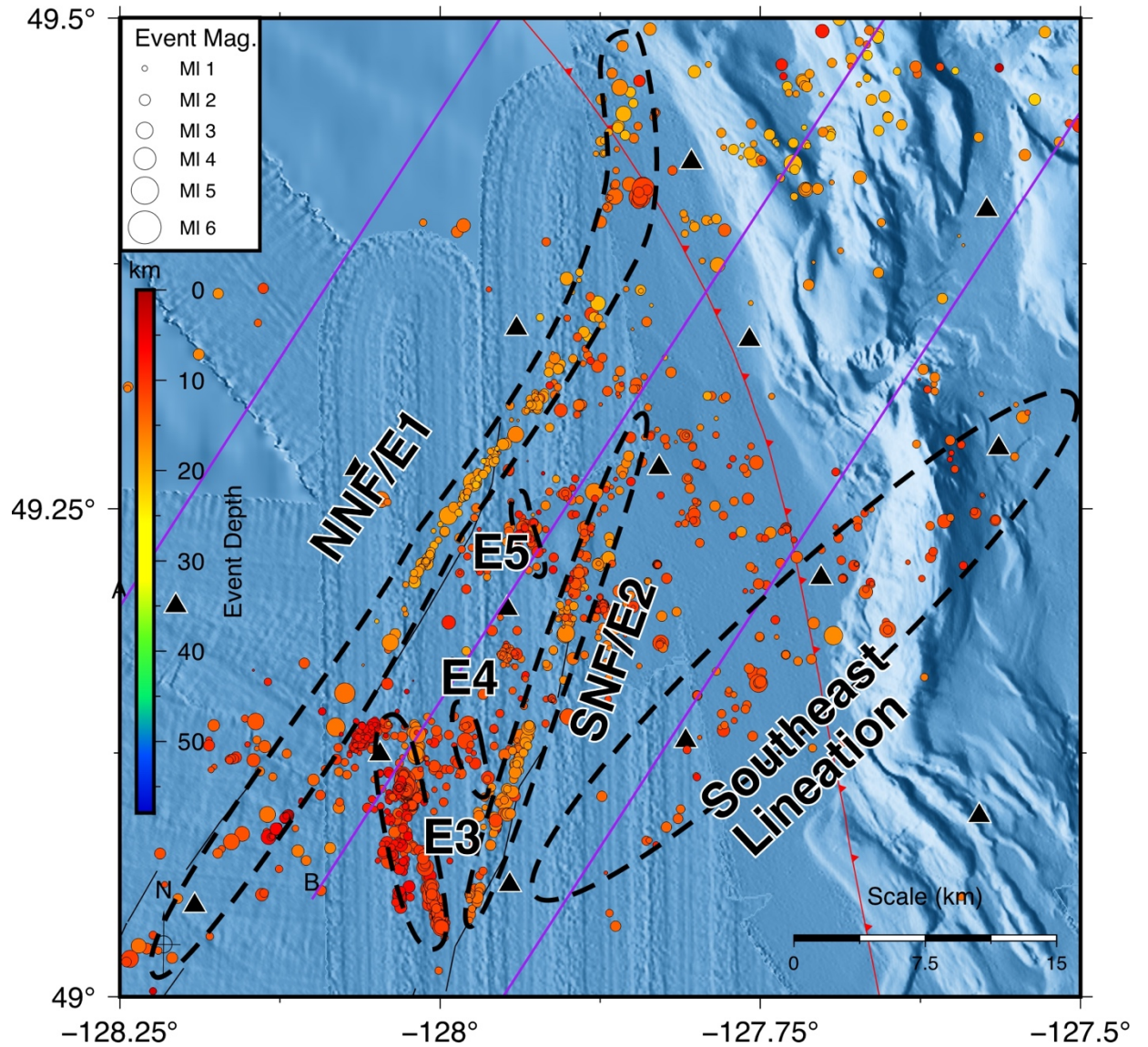to determine the best fit G-R distributions.

Figure 3. Detailed map of hypocentres focused on the Nootka fault zone. Purple lines are vertical transects shown in Figure 6. Seismic features, including faults and more diffuse lineations, are outlined with black dashed lines and labelled after the conventions established in (Hutchinson et al., 2019). E1 and E2 are also labelled NNF and SNF, for northwestern and southeastern Nootka faults, after Rohr et al. (2018). See Figure 1 for the explanation of other features on the map.
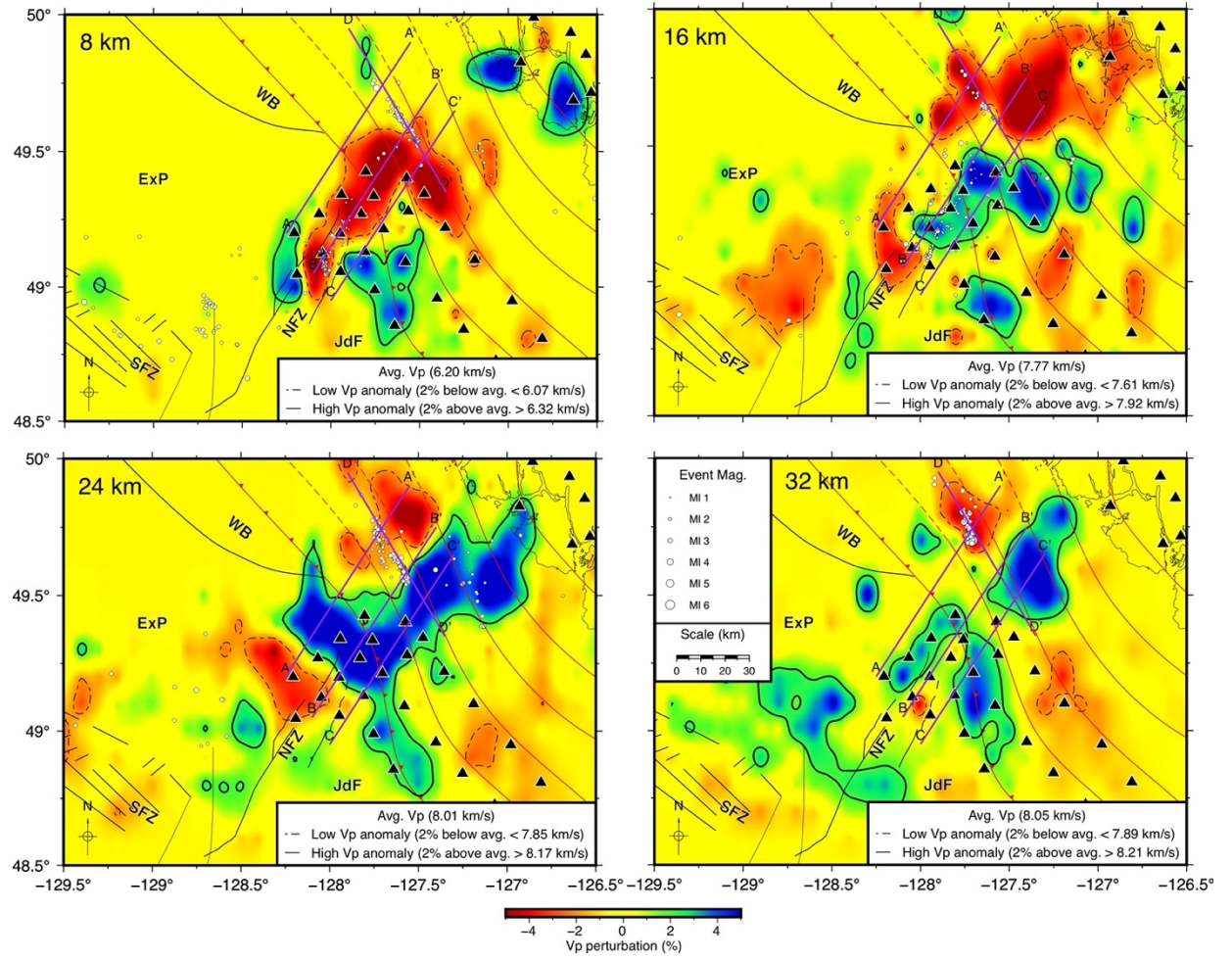
Figure 4. Depth slices of Vp of seismic tomography. From the upper left to the lower right, depths increase by 8 km intervals from 8-32 km. Hypocentres within a vertical distance of 1 km are shown as white-filled circles, with size indicating magnitude. Velocity anomalies are contoured where they are 2% above or below mean P-velocities for the depth slice. Low and high velocity anomalies are indicated by red and blue colours, as well as by dashed and solid contours, respectively. The purple lines show the locations of vertical cross-sections in Figure 6. See Figure 1 for the explanation of other features on the map.
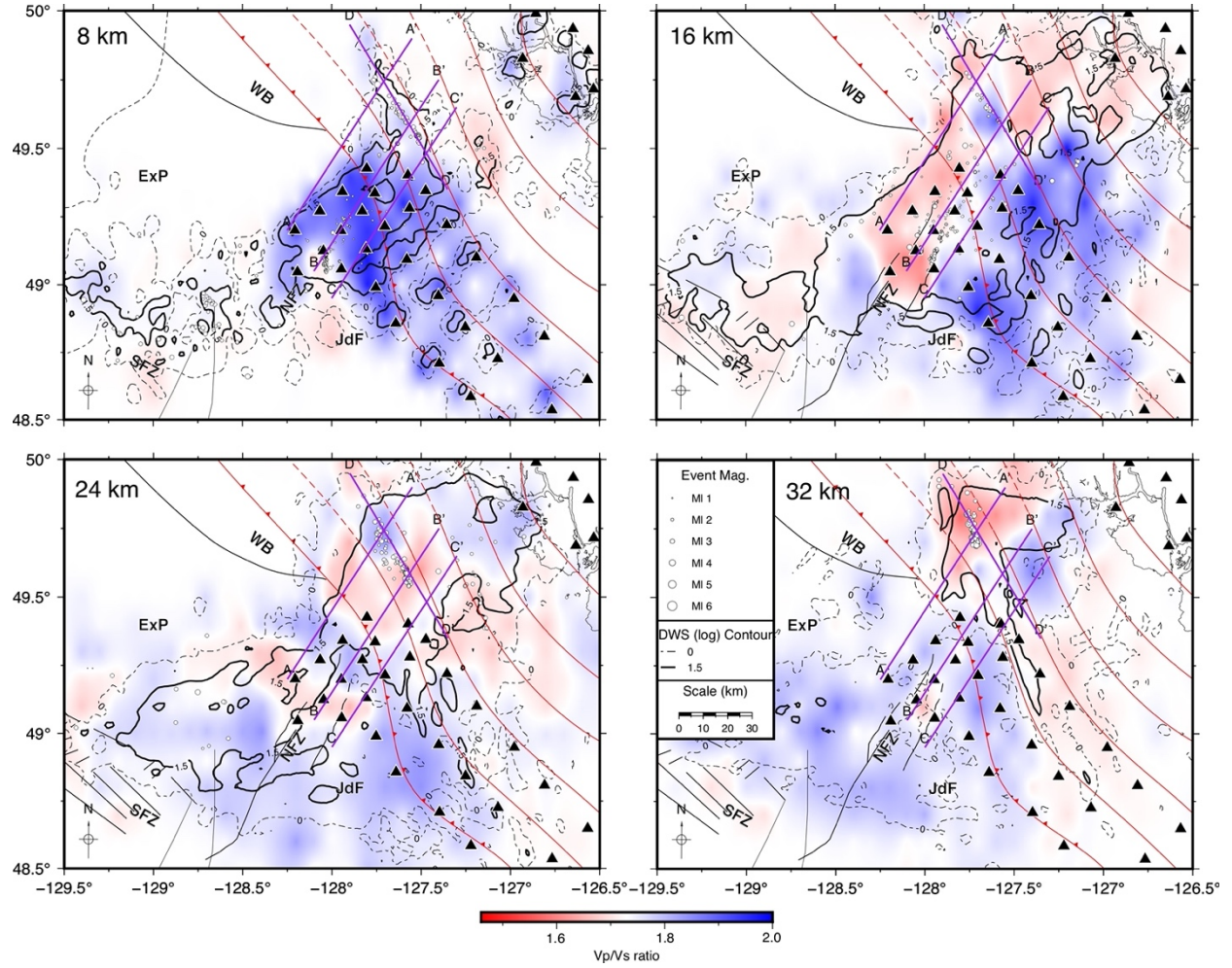
20

Figure 5. Depth slices of V_p/V_s seismic tomography at the same depths as Figure 4. V_p/V_s ratios greater than or less than 1.73 are shown as blue and red, respectively. DWS contours illustrate areas of high raypath densities and typically indicate where the tomography is best resolved. See Figures 1 and 4 for the explanation of other features on the map.
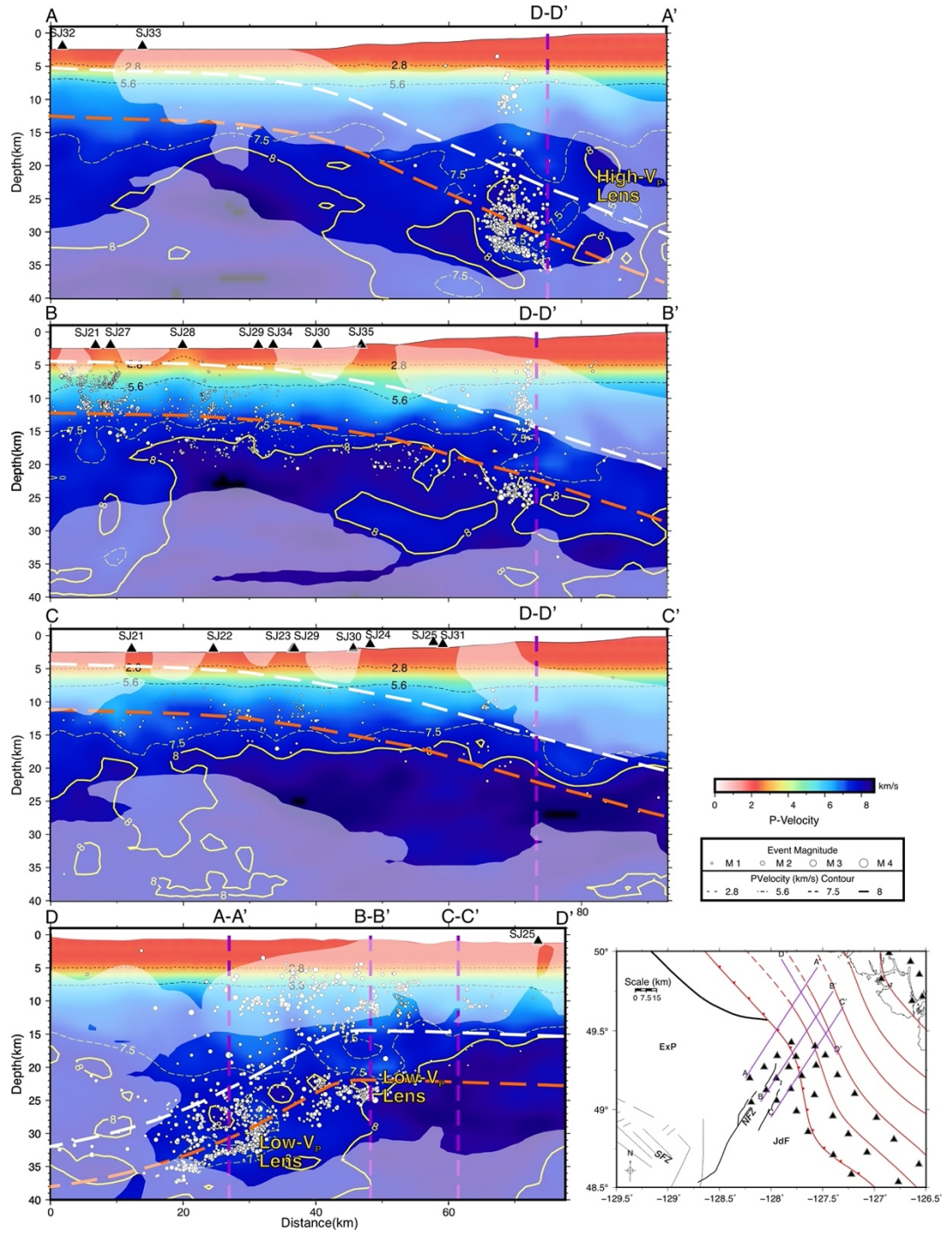
Figure 6. Cross-section profiles of Vp seismic tomography. Earthquakes within 5

km of the profiles are projected and marked as white-filled circles, while stations within 10 km of the profiles are marked as red triangles. Vp contours are shown as back and yellow lines labeled with representative *P*-velocities. A reference map for the study area and the profile lines are shown in the lower right corner. Cross-section intersections are shown with dashed purple lines and are labelled accordingly. White and orange dashed lines are representative of the inferred top of the oceanic plate and oceanic Moho, respectively, based on Hutchinson et al. (2020) and Hutchinson et al. (2019). Translucent white overlays indicate areas of lower raypath density corresponding to the log value of the DWS.
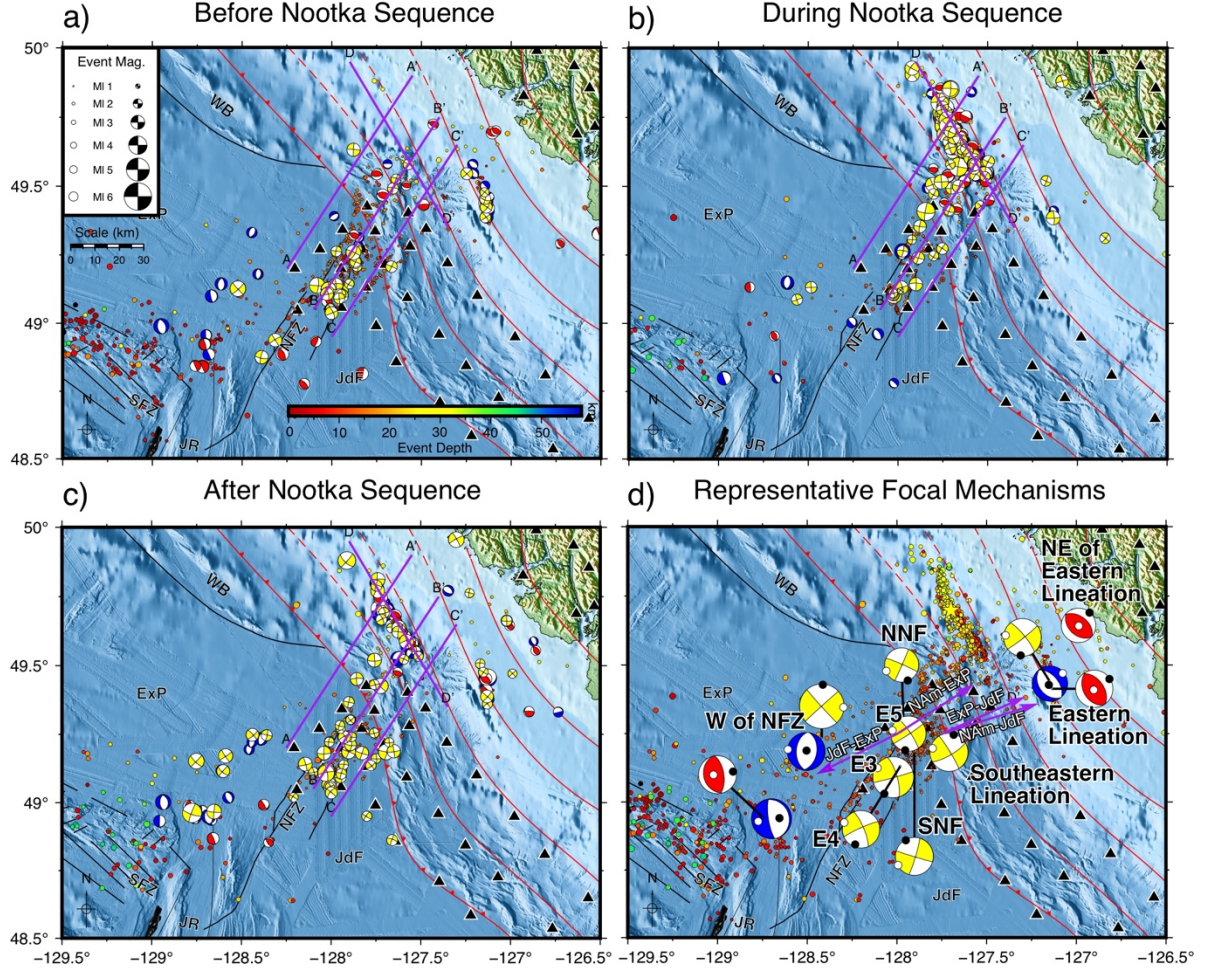

Figure 7. Maps of focal mechanism solutions from before (a), during (b), and after (c) the Nootka Sequence. Representative averaged focal mechanism solutions from all three time windows are shown in (d) and are given in Table 2. The sizes of the focal mechanisms are indicative of M_L while colour represents rupture type; red = reverse, blue = normal, yellow = strike-slip. The purple

arrows in (d) show relative plate motions between pairs of plates; the labels indicate the motion of the second plate relative to the first. Plate motions involving the ExP were calculated with model A of Braunmiller and Nábělek, 2002, while all others were calculated with NUVEL-1A. ExP – Explorer plate, JdF – Juan de Fuca plate, SFZ – Sovanco fracture zone, NFZ – Nootka fault zone, JR – Juan de Fuca Ridge, WB – Winona Block. Representative focal mechanisms sizes have a scale 3 times that in the other diagrams. See Figure 1 for the explanation of other features on the map.
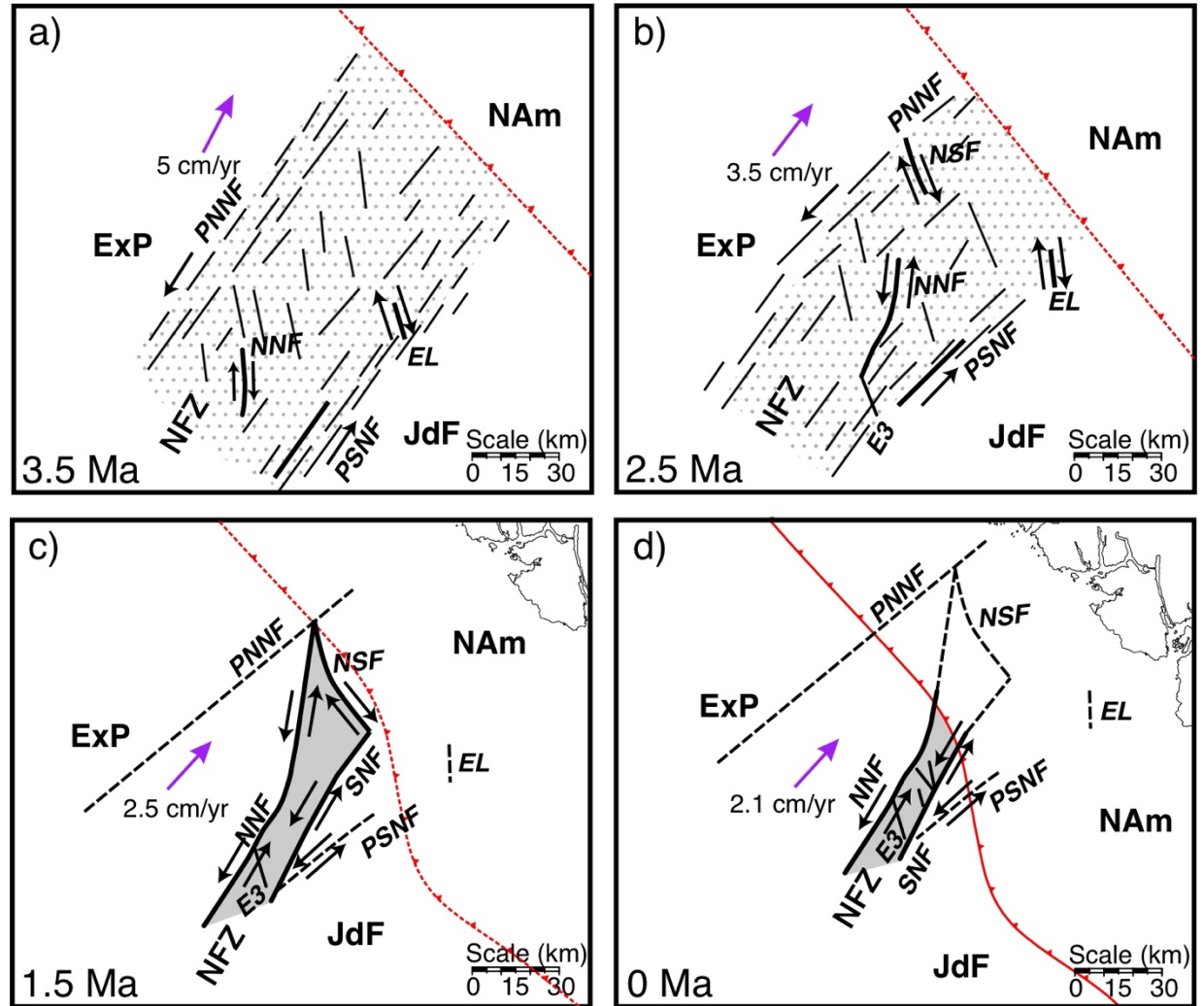

Figure 8. Illustrative diagram of the presumed evolution of the Nootka fault zone from 3.5 Ma (a) to 0 Ma (d). At 3.5 Ma, the Nootka fault zone begins as a region of distributed shear between the Explorer and Juan de Fuca plates. Clockwise rotation occurs between ~ 3.5 Ma and 1.5 Ma. The subduction front

has presumably developed with the deposition of sediments, so the exact configuration prior to 0 Ma is unknown. Relative motions along faults are indicated by opposing black arrows. Areas of distributed shear are indicated by gray stippling. Solid gray regions indicate that shear dislocation only happens along individual faults. Purple arrows show the relative motion of the Explorer plate relative to North America. Text labels are abbreviations for the following features; ExP – Explorer plate, JdF – Juan de Fuca plate, NFZ – Nootka fault zone, PNNF – paleo-northwestern Nootka fault, SNNF – paleo-southeastern Nootka fault, NNF – northwestern Nootka fault, SNF – southeastern Nootka fault, EL – eastern lineation, NSF – Nootka Sequence fault, NAM – North America plate.

Table 1. Hypocentre lineations/zones and associated attributes.

Lineation/Zone	Strike	Dip	Lineation Length (km)	Lineation Width (
E1 or NNF[1,2]	33.3° ± 0.4°	81.1° ± 2.8°	~30	0.9
E1 NE	13.9° ± 1.7°		17	3
E2 or SNF[3]	198.8° ± 0.3°	81.2 ± 1.3	29	1.5
E3	163.3° ± 0.1°	80.9° ± 1.4°	9.3	0.8
E4	153.2° ± 1.4°	74.2° ± 2.6°	9.7	1.7
E5	152.1° ± 1.0°	82.8 ± 3.1	9.4	1.7
Eastern Lineation	170° ± 2.4°	84.7° ± 0.7°	17	3
Southeastern Lineation	43.8° ± 1.2°	Too Diffuse	37	9
ExP Strike-Slip	49.5° ± 1.9°	Too Diffuse	47	11
ExP	N/A	N/A	N/A	N/A
JdF	N/A	N/A	N/A	N/A
NW Nootka Sequence	157.7° ± 0.5°	Nearly Vertical	24.7	3 - 6.5
SE Nootka Sequence	142.1° ± 0.4°	Nearly Vertical	29.3	3 - 6.5

[1] Near to the subduction front, the NNF appears to change direction to a more northerly strike. Due to the small number of earthquakes, the strike has not been calculated.

[2] NNF is an abbreviation for the northwestern Nootka fault.

[3] SNF is an abbreviation for the southeastern Nootka fault.

Table 2. Representative average focal mechanism solutions for selected areas.

Zone	Strike (°)	Dip (°)	Rake (°)	Aux-Strike (°)	Aux-Dip (°)	Aux-Ra
W of NFZ[1]	9.6	43.7	-84.6	182.2	46.6	-95.1
W of NFZ (further SW)	171.1	76.9	-86.7	336.7	13.6	-104.0
NE of Eastern Lineation[2]	308.3	47.3	86.5	133.4	42.8	93.8
Eastern Lineation	51.6	85.8	10.8	320.8	79.2	175.8
Eastern Lineation	142.7	37.0	-87.8	319.9	53.0	-91.7
Eastern Lineation	331.3	53.6	97.6	138.7	37.1	79.9
SE Lineation	59.8	76.9	4.9	328.7	85.2	166.8

Zone	Strike (°)	Dip (°)	Rake (°)	Aux-Strike (°)	Aux-Dip (°)	Aux-Ra
NNF	23.7	88.6	3.8	293.6	86.2	178.6
SNF	16.7	85.0	-1.4	106.8	88.6	-175.0
E3	74.4	88.0	15.2	343.9	74.8	178.0
E4	245.8	83.7	-12.3	337.1	77.8	-173.6
E5	56.4	86.5	9.4	325.8	80.7	176.5
Relict Slip Zone[3]	227.9	89.0	1.8	137.8	88.2	179.0
Western Reverse Faults[4]	351.1	62.6	92.9	164.8	27.5	84.4

[1] Located within the vicinity of 49.15° N, 128.5° W.

[2] Located within the vicinity of 49.7° N, 127° W.

[3] Located within the vicinity of 49.25° N, 128.5° W

[4] Located within the vicinity of 48.8° N, 128.75° W

[5] Rupture classification type is labelled as follows: N – normal, R – reverse, S – strike-slip

References

Aki, K., and P. G. Richards, 2002, Quantitative seismology, 2nd Edition, University Science Books, 700 p.Álvarez-Gómez, J. A., 2019, FMC—Earthquake focal mechanisms data management, cluster and classification, SoftwareX, 9, 299–307, doi: 10.1016/j.softx.2019.03.008.Atwater, T., 1970, Implications of plate tectonics for the cenozoic tectonic evolution of western north america, Bulletin of the Geological Society of America, 81, no. 12, 3513–3536, doi: 10.1130/0016-7606(1970)81[3513:IOPTFT]2.0.CO;2.Atwater, B. F., S. Musumi-Rokkaku, K. Satake, Y. Tsuji, K. Ueda, and D. K. Yamaguchi, 2015, The orphan tsunami of 1700—Japanese clues to a parent earthquake in North America, Seattle, University of Washington Pressal Survey, U.S. Geological Survey Professional Paper 1707, 135 p.Braunmiller, J., and J. Nábělek, 2002, Seismotectonics of the Explorer region, Journal of Geophysical Research: Solid Earth, 107, no. B10, 1-1—1-25, doi: 10.1029/2001jb000220.Brothers, D. S., N. C. Miller, J. V. Barrie, P. J. Haeussler, H. G. Greene, B. D. Andrews, O. Zielke, J. Watt, and P. Dartnell, 2020, Plate boundary localization, slip-rates and rupture segmentation of the Queen Charlotte Fault based on submarine tectonic geomorphology, Earth and Planetary Science Letters, 530, 16, doi: 10.1016/j.epsl.2019.115882.Cao, A., and S. S. Gao, 2002, Temporal variation of seismic b -values beneath northeastern Japan island arc, Geophysical Research Letters, 29, no. 9, 48-1—48-3, doi: 10.1029/2001gl013775.Clowes, R. M., A. J. Thorleifson, and S. Lynch, 1981, Winona Basin, west coast Canada: crustal structure from marine seismic studies., Journal of Geophysical Research, 86, no. B1, 225–242, doi: 10.1029/JB086iB01p00225.Davis, E. E., and R. P. Riddihough, 1982, The Winona Basin: structure and tectonics, Canadian

Journal of Earth Sciences, 19, no. 4, 767–788, doi: 10.1139/e82-065.DeMets, C., R. G. Gordon, and D. F. Argus, 2010, Geologically current plate motions, Geophysical Journal International, 181, no. 1, 1–80, doi: 10.1111/j.1365-246X.2009.04491.x.DeMets, C., R. G. Gordon, D. F. Argus, and S. Stein, 1994, Effect of recent revisions to the geomagnetic reversal time scale on estimates of current plate motions, Geophysical Research Letters, 21, no. 20, 2191–2194, doi: 10.1029/94GL02118.DeMets, C., and S. Merkouriev, 2016, High-resolution reconstructions of Pacific-North America plate motion: 20 Ma to present, Geophysical Journal International, 207, no. 2, 741–773, doi: 10.1093/gji/ggw305.Eberhart-Phillips, D., 1990, Three-dimensional P and S velocity structure in the Coalinga Region, California, Journal of Geophysical Research, 95, no. B10, 15343–15363, doi: 10.1029/jb095ib10p15343.Gao, D., 2016, Defining megathrust tsunami sources at northernmost Cascadia using thermal and structural information, MSc Thesis, University of Victoria, Canada.Gao, D., K. Wang, E. E. Davis, Y. Jiang, T. L. Insua, and J. He, 2017, Thermal state of the Explorer segment of the Cascadia subduction zone: Implications for seismic and tsunami hazards, Geochemistry, Geophysics, Geosystems, 18, no. 4, 1569–1579, doi: 10.1002/2017GC006838.Hardebeck, J. L., and P. M. Shearer, 2002, A new method for determining first-motion focal mechanisms, Bulletin of the Seismological Society of America, 92, no. 6, 2264–2276, doi: 10.1785/0120010200.Hardebeck, J. L., and P. M. Shearer, 2003, Using S/P amplitude ratios to constrain the focal mechanisms of small earthquakes, Bulletin of the Seismological Society of America, 93, no. 6, 2434–2444, doi: 10.1785/0120020236.Hole, J. A., and B. C. Zelt, 1995, 3-D finite-difference reflection travel times, Geophysical Journal International, 121, no. 2, 427–434, doi: 10.1111/j.1365-246X.1995.tb05723.x.Hutchinson, J., 2021, Tectonic evolution of the Nootka fault zone and deformation of the shallow subducted Explorer plate in northern Cascadia as revealed by earthquake distributions and seismic tomography data, OSF, doi: 10.17605/OSF.IO/5Q9FB.Hutchinson, J., H. Kao, M. Riedel, K. Obana, K. Wang, S. Kodaira, T. Takahashi, and Y. Yamamoto, 2020, Significant geometric variation of the subducted plate beneath the northernmost Cascadia subduction zone and its tectonic implications as revealed by the 2014 MW 6.4 earthquake sequence, Earth and Planetary Science Letters, 551, 116569, doi: 10.1016/j.epsl.2020.116569.Hutchinson, J., H. Kao, G. Spence, K. Obana, K. Wang, and S. Kodaira, 2019, Seismic characteristics of the nootka fault zone: Results from the seafloor earthquake array Japan–Canada cascadia experiment (seajade), Bulletin of the Seismological Society of America, 109, no. 6, 2252–2276, doi: 10.1785/0120190008.Kao, H., Y. Behr, C. A. Currie, R. Hyndman, J. Townend, F. C. Lin, M. H. Ritzwoller, S. J. Shan, and J. He, 2013, Ambient seismic noise tomography of Canada and adjacent regions: Part I. Crustal structures, Journal of Geophysical Research: Solid Earth, 118, no. 11, 5865–5887, doi: 10.1002/2013JB010535.Krischer, L., T. Megies, R. Barsch, M. Beyreuther, T. Lecocq, C. Caudron, and J. Wassermann, 2015, ObsPy: a bridge for seismology into the scientific Python ecosystem, Computational Science & Discovery, 8, no. 1, 014003, doi: 10.1088/1749-4699/8/1/014003.Mosher, S. G., P. Audet, and I. L'Heureux,

2014, Seismic evidence for rotating mantle flow around subducting slab edge associated with oceanic microplate capture, Geophysical Research Letters, 41, no. 13, 4548–4553, doi: 10.1002/2014GL060630.Pavlis, G. L., F. Vernon, D. Harvey, and D. Quinlan, 2004, The generalized earthquake-location (GENLOC) package: an earthquake-location library, Computers & Geosciences, 30, nos. 9–10, 1079–1091, doi: 10.1016/j.cageo.2004.06.010.Riddihough, R. P., 1984, Recent Movements of the Juan de Fuca Plate System, Journal of Geophysical Research, 89, no. B8, 6980–6994, doi: 10.1029/JB089iB08p06980.Riddihough, R. P., R. G. Currie, and R. D. Hyndman, 1980, The Dellwood Knolls and their role in triple junction tectonics off northern Vancouver Island, Canadian journal of earth sciences, 17, no. 5, 577–593, doi: 10.1139/e80-057.Rohr, K. M. M., K. P. Furlong, and M. Riedel, 2018, Initiation of Strike-Slip Faults, Serpentinization, and Methane: The Nootka Fault Zone, the Juan de Fuca-Explorer Plate Boundary, Geochemistry, Geophysics, Geosystems, 19, no. 11, 4290–4312, doi: 10.1029/2018GC007851.Rohr, K., A. T.- Geochemistry, undefined Geophysics, undefined Geosystems, and undefined 2010, 2010, Pacific-North America plate boundary reorganization in response to a change in relative plate motion: Offshore Canada, Wiley Online Library, 11, no. 6, doi: 10.1029/2009GC003019.Ross, Z. E., and Y. Ben-Zion, 2014, Automatic picking of direct P, S seismic phases and fault zone head waves, Geophysical Journal International, 199, no. 1, 368–381, doi: 10.1093/gji/ggu267.Ryan, W. B. F. et al., 2009, Global multi-resolution topography synthesis, Geochemistry, Geophysics, Geosystems, 10, no. 3, 1–9, doi: 10.1029/2008GC002332.Satake, K., 2003, Fault slip and seismic moment of the 1700 Cascadia earthquake inferred from Japanese tsunami descriptions, Journal of Geophysical Research, 108, no. B11, 2535, doi: 10.1029/2003JB002521.Savard, G., M. G. Bostock, J. Hutchinson, H. Kao, N. I. Christensen, and S. M. Peacock, 2020, The Northern Terminus of Cascadia Subduction, Journal of Geophysical Research: Solid Earth, 125, no. 6, doi: 10.1029/2019JB018453.Stubailo, I., 2015, Seismic anisotropy below Mexico and its implications for mantle dynamics, PhD Thesis, UCLA.Sypus, M., 2019, Models of tsunamigenic earthquake rupture along the west coast of North America.Toomey, D. R. et al., 2014, The Cascadia initiative: A sea change in seismological studies of subduction zones, Oceanography, 27, no. 2, 138–150, doi: 10.5670/oceanog.2014.49.Wagner, L. S., S. Beck, and G. Zandt, 2005, Upper mantle structure in the south central Chilean subduction zone (30° to 36°S), Journal of Geophysical Research: Solid Earth, 110, no. 1, 1–20, doi: 10.1029/2004JB003238.Waldhauser, F., 2001, HypoDD–A program to compute double-difference hypocenter locations, US Geol. Surv. Open File Rep., 01, 113, 1–25, doi: 10.7916/D8SN072H.Wang, K., and A. M. Tréhu, 2016, Invited review paper: Some outstanding issues in the study of great megathrust earthquakes—The Cascadia example, Journal of Geodynamics, 98, 1–18, doi: 10.1016/j.jog.2016.03.010.Wassermann, J., R. Barsch, M. Beyreuther, Y. Behr, T. Megies, and L. Krischer, 2010, ObsPy: A Python Toolbox for Seismology, Seismological Research Letters, 81, no. 3, 530–533, doi: 10.1785/gssrl.81.3.530.Wessel, P., and W. H. F. Smith, 1998, New, improved version of generic mapping tools released, Eos, Transactions American

Geophysical Union, 79, no. 47, 579–579, doi: 10.1029/98eo00426.Zhang, H., and C. Thurber, 2006, Development and applications of double-difference seismic tomography, Pure and Applied Geophysics, 163, nos. 2–3, 373–403, doi: 10.1007/s00024-005-0021-y.

Tectonic evolution of the Nootka fault zone and deformation of the shallow subducted Explorer plate in northern Cascadia as revealed by earthquake distributions and seismic tomography

Jesse Hutchinson[1,5], Honn Kao[1,2], Michael Riedel[3], Koichiro Obana[4], Kelin Wang[1,2], Shuichi Kodaira[4], Tsutomu Takahashi[4], and Yojiro Yamamoto[4]

[1] School of Earth and Ocean Sciences, University of Victoria, Victoria, BC, V8P 5C2, Canada

[2] Pacific Geoscience Centre, Geological Survey of Canada, Natural Resources Canada, Sidney, BC, V8L 4B2, Canada

[3] GEOMAR Helmholtz-Centre for Ocean Research Kiel, Kiel, Germany

[4] Japan Agency for Marine-Earth Science and Technology (JAMSTEC), Yokohama, Japan

[5] Now at the Univeristy of Canterbury, New Zealand.

Contents of this file

Text SA to SC
Figures S1 to S3

Additional Supporting Information (Files available separately)

Captions for Tables A1 to C2

Introduction

This document includes supporting information for supplemental tables, figures, and text. The supplemental tables A1, A2, B1, C1, and C2 include earthquake arrival, earthquake hypocentre, focal mechanism solutions, P-velocity tomography, and S-velocity tomography respectively. Figures S1 – S3 provide seismic tomography checkerboard test results, detailed P-velocity tomography maps, and P-velocity % perturbation tomography profiles. The supplemental text details information about the focal mechanism solutions and TomoDD procedures.

Text SA Earthquake Datasets

Data used in the earthquake arrival and hypocentre tables are available from the Open Science Forum at (https://osf.io/5q9fb/?view_only=f67fbfee2011466ab879e547adb982fb). Descriptions are detailed in the captions for tables A1 and A2.

Text SB Focal Mechanism Datasets

Focal mechanism solutions were computed with the program HASH (Hardebeck and Shearer, 2002, 2003). Like many programs used to calculate focal mechanism solutions (e.g. FPFIT; Reasenberg and Oppenheimer, 1985), HASH calculates the best-fit solutions for earthquakes from input *P*-arrival first motions. An additional benefit of HASH is that *S/P* amplitude ratios can be utilized to further constrain focal mechanism solutions. Theoretically, *P* amplitudes along nodal planes would be the smallest, while they would be the largest at the P and T axes. Therefore, *S/P* ratios are expected to be much larger along nodal planes than within focal sphere quadrants.

Several factors are utilized for determining the quality of a best-fit focal mechanism solution, which is ranked from A-F, with A being the best. Any focal mechanisms with fewer than 8 first motion polarities are given an F rank. Solutions with azimuthal gaps > 90° and takeoff angle gaps > 60° are given an E rank. Any solution with smaller gaps is considered at least a D-ranked solution. Higher ranks are given with smaller average misfits and RMS fault plane uncertainties, and larger station distribution ratios and focal mechanism probabilities. For a given earthquake, these values are determined from a set of focal mechanisms calculated over repeated trials. Ultimately, an A-ranked focal mechanism solution has an average misfit ≤ 0.15, an RMS fault plane uncertainty ≤ 25°, a station distribution ratio ≥ 0.5, a mechanism probability ≥ 0.8, a maximum azimuthal gap ≤ 90°, a maximum takeoff angle gap ≤ 60°, and 8 or more first-motion polarities.

The focal mechanism data described for the tables below are available from the Open Science Forum at (https://osf.io/5q9fb/?view_only=f67fbfee2011466ab879e547adb982fb). Descriptions are detailed in the captions for table B1.

Text SC Tomography Datasets.

TomoDD parameters from the TomoDD input file for the combined SeaJade I and II dataset are listed below. Note that the parameters are described in the documentation for both HypoDD (Waldhauser, 2001) and TomoDD (Zhang and Thurber, 2006). Descriptions for the TomoDD velocity model data tables are provided following the input parameter information.

```
*--- input file selection
* cross correlation diff times:
./new_dt_mincorr_08.cc
*
*catalog P diff times:
./new_dt.ct
* catalog absolute times
./new_absolute.dat
*
* event file:
./new_events.dat
*
```

```
* station file:
./new_station.dat
*
*--- output file selection
* original locations:
tomodd_seajade_02.loc
* relocations:
tomodd_seajade_02.reloc
* station information:
tomodd_seajade_02.sta
* residual information:
tomodd_seajade_02.res
* source paramater information:
tomodd_seajade_02.src
*Output velocity
tomodd_seajade_02.vel
* Vp model
Vp_model_02.dat
* Vs model
Vs_model_02.dat
*--- data type selection:
* IDAT:  0 = synthetics; 1= cross corr; 2= catalog; 3= cross & cat
* IPHA: 1= P; 2= S; 3= P&S
* DIST:max dist [km] between cluster centroid and station
* IDAT   IPHA   DIST
   3      3     400
*
*--- event clustering:
* OBSCC:    min # of obs/pair for crosstime data (0= no clustering)
* OBSCT:    min # of obs/pair for network data (0= no clustering)
* OBSCC  OBSCT  CC_format
    8      8      1
*
*--- solution control:
* ISTART:   1 = from single source; 2 = from network sources
* ISOLV:    1 = SVD, 2=lsqr
* NSET:         number of sets of iteration with specifications
following
*  ISTART  ISOLV  NSET weight1 weight2 weight3 air_depth
    2       2      18    15       15       15      -1.5
* i3D delt1 ndip iskip scale1 scale2 iuses
   2    0    9    1     0.5    1.00    2
* xfac   tlim     nitpb(1) nitpb(2) stepl
  1.3   0.0005    50        50       0.5
* lat_Orig lon_Orig Z_Orig iorig rota
   49.25  -127.75    0       1     0
*
*--- data weighting and re-weighting:
* NITER:         last iteration to used the following weights
* WTCCP, WTCCS:       weight cross P, S
* WTCTP, WTCTS:       weight catalog P, S
* WRCC, WRCT:         residual threshold in sec for cross, catalog
data
* WDCC, WDCT:         max dist [km] between cross, catalog linked
pairs
```
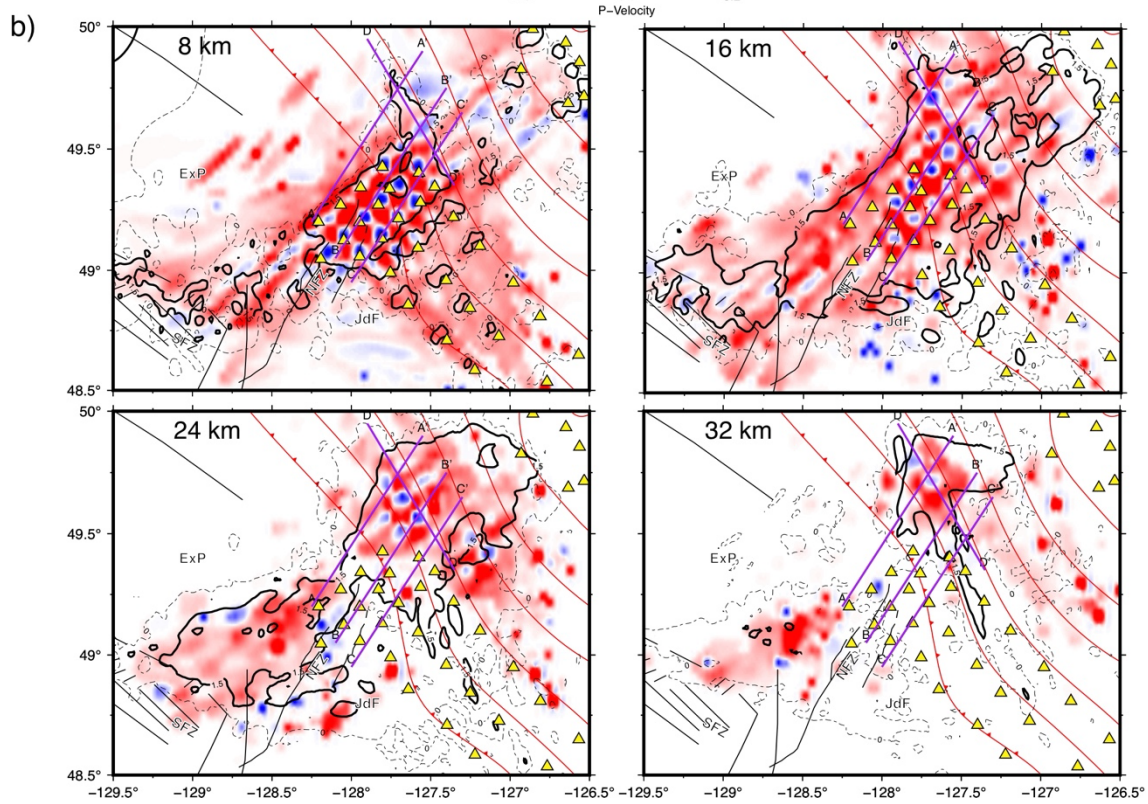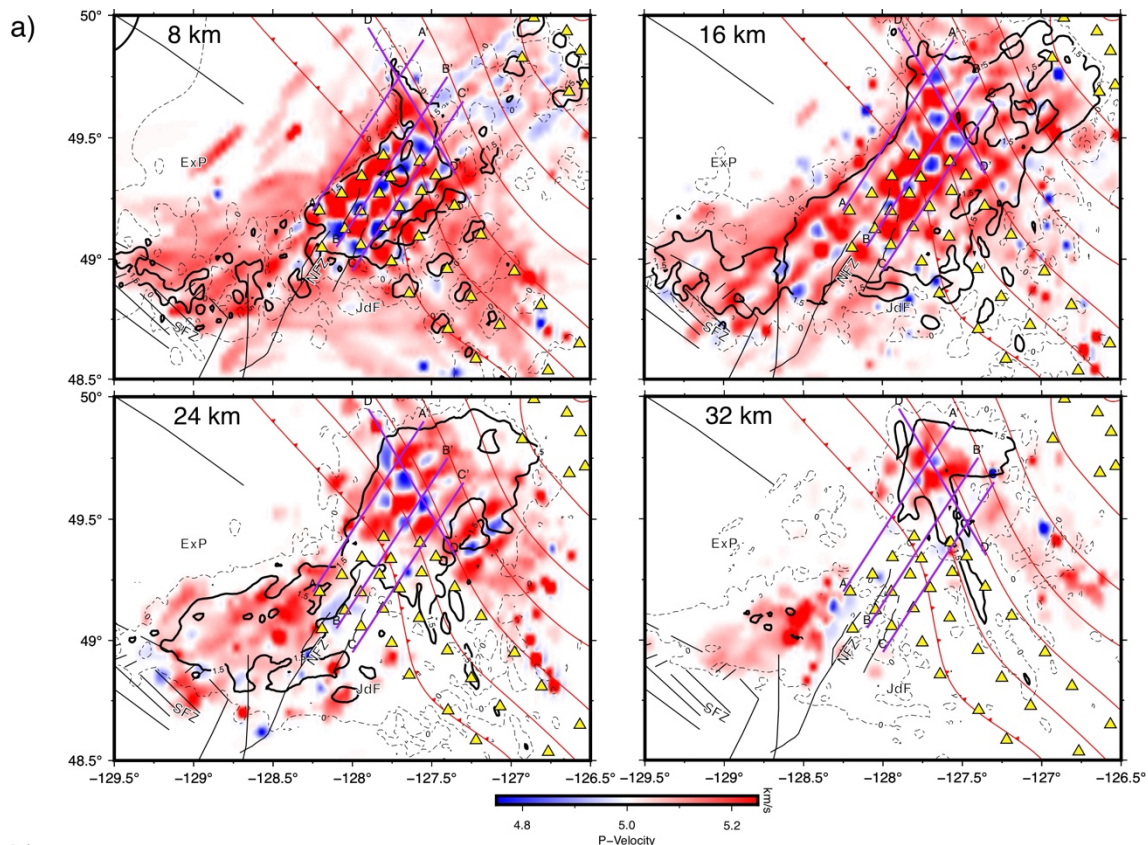
```
* WTCD:   relative weighting between absolute and differential data
* THRES: Scalar used to determine the DWS threshold values
* DAMP:          damping (for lsqr only)
*        --- CROSS DATA ----- ----CATALOG DATA ----
* NITER WTCCP WTCCS WRCC  WDCC   WTCTP  WTCTS WRCT WDCT WTCD DAMP JOINT
THRES
  5     0.1   0.05  -9    -9     0.5    0.25  -9   20   1    350  0
0.2
  3     0.1   0.05  -9    -9     0.5    0.25  -9   20   1    350  1
0.2
  5     0.1   0.05  -9    -9     0.5    0.25  -9   20   1    350  0
0.2
  5     0.1   0.05  6     10     0.1    0.05  6    10   1    350  0
0.2
  3     0.1   0.05  6     10     0.1    0.05  6    10   1    350  1
0.2
  5     0.1   0.05  6     10     0.1    0.05  6    10   1    350  0
0.2
  5     1.0   0.5   6     5      0.1    0.05  6    5    0.1  300  0
0.2
  3     1.0   0.5   6     5      0.1    0.05  6    5    0.1  300  1
0.2
  5     1.0   0.5   6     5      0.1    0.05  6    5    0.1  300  0
0.2
  5     1.0   0.5   6     2      0.01   0.005 6    2    0.1  300  0
0.2
  3     1.0   0.5   6     2      0.01   0.005 6    2    0.1  300  1
0.2
  5     1.0   0.5   6     2      0.01   0.005 6    2    0.1  300  0
0.2
  5     1.0   0.5   6     1      0.01   0.005 6    2    0.1  300  0
0.2
  3     1.0   0.5   6     1      0.01   0.005 6    2    0.1  300  1
0.2
  5     1.0   0.5   6     1      0.01   0.005 6    2    0.1  300  0
0.2
  5     1.0   0.5   6     0.5    0.01   0.005 6    2    0.1  300  0
0.2
  3     1.0   0.5   6     0.5    0.01   0.005 6    2    0.1  300  1
0.2
  5     1.0   0.5   6     0.5    0.01   0.005 6    2    0.1  300  0
0.2
*
*--- event selection:
* CID:      cluster to be relocated (0 = all)
* ID: cuspids of event to be relocated (8 per line)
* CID
    1
* ID
```

Seismic tomography data tables are available from the Open Science Forum at (https://osf.io/5q9fb/?view_only=f67fbfee2011466ab879e547adb982fb). Descriptions are detailed in the captions for tables C1 and C2.
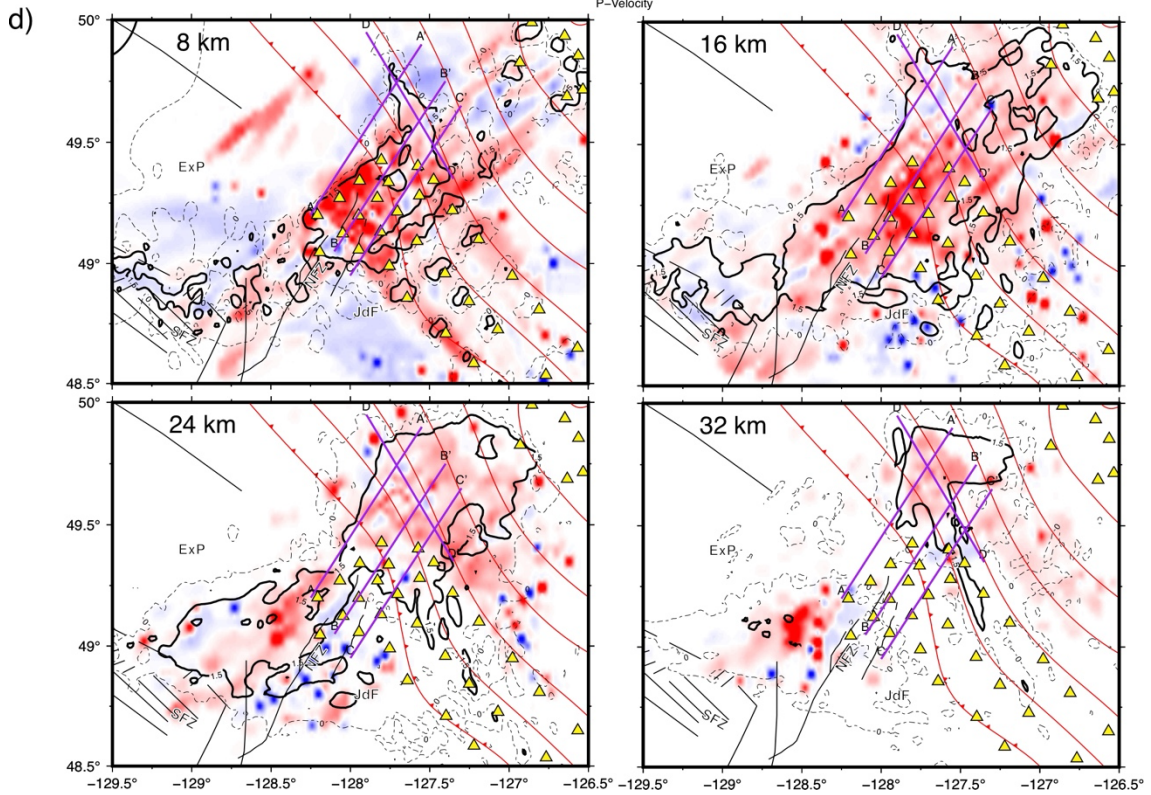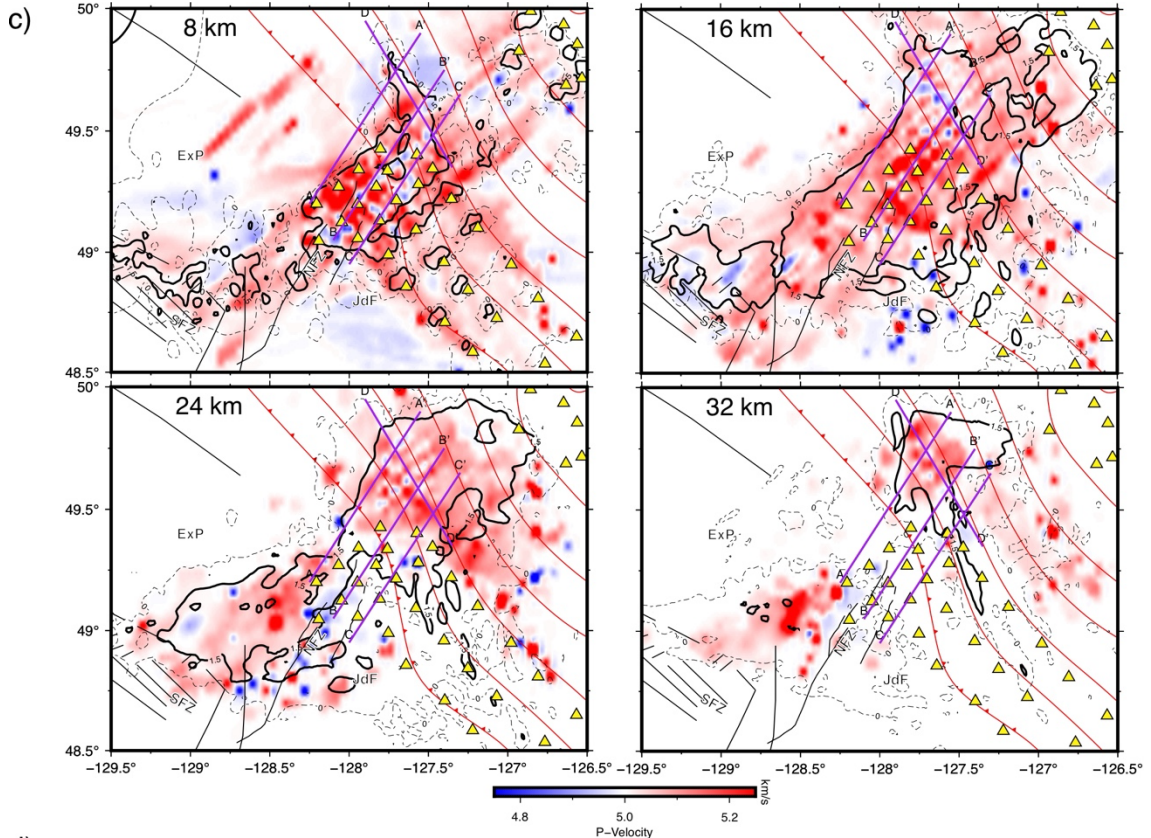
Figure S1. Maps of checkerboard tomography resolution tests. Tests at depths of 8, 16, 24, and 32 km are shown for resolutions of a) 10-km, b) 8-km, c) 5-km, and d) 3-km.
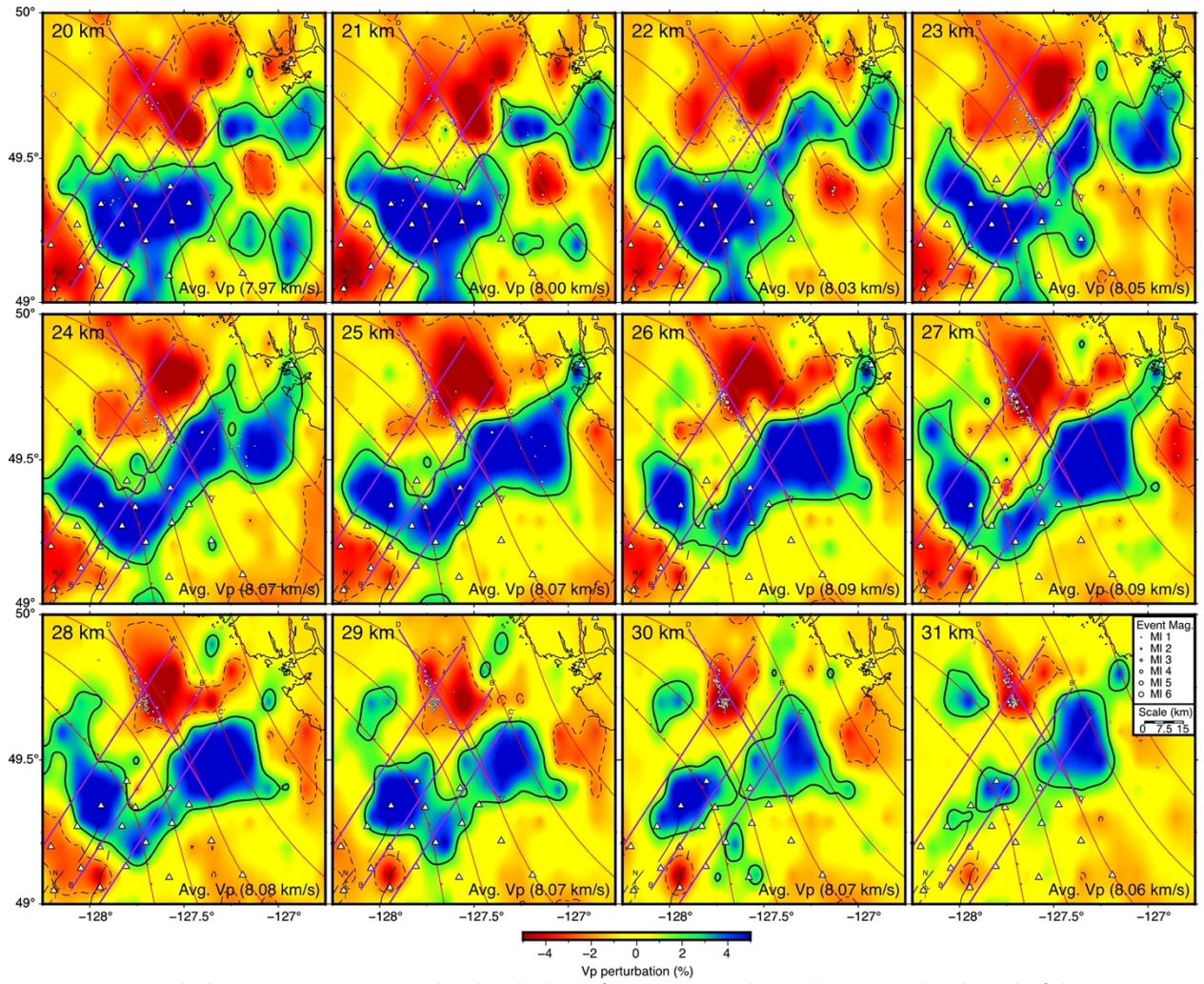
6

Figure S2. Detailed V$_P$ seismic tomography depth slices focusing mainly on the region landward of the subduction front.
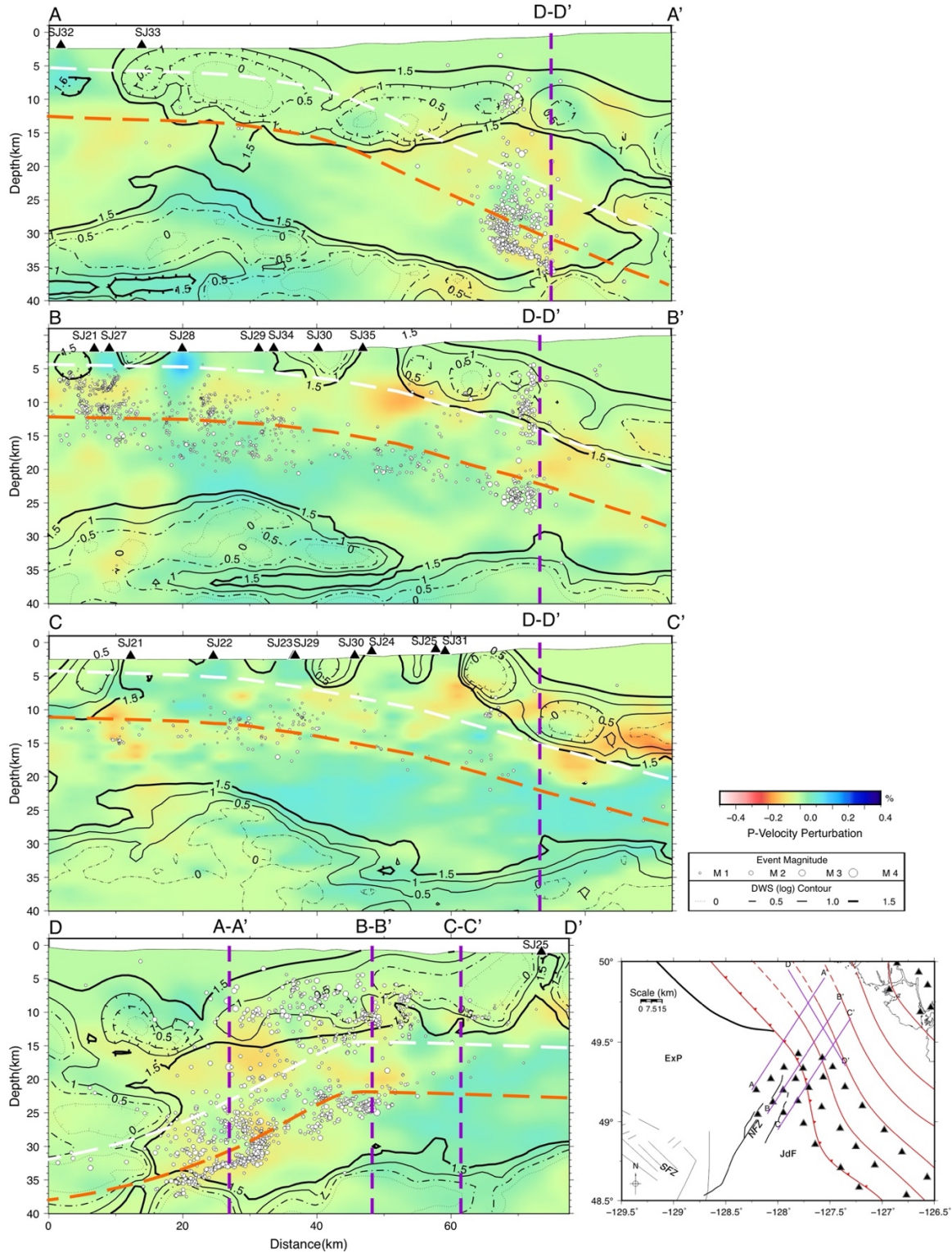
Figure S3. Cross-section profiles of seismic tomography with raypath density DWS contours. Seismic tomography is presented in the % perturbation of V_P from the initial 1-D velocity model (Spence et al., 1985). Earthquakes within 5 km of the profiles are projected and marked as white-filled circles, while stat within 10 km of the profile etc. [see Figure 7 caption]. A reference map for the study area and the profile lines is shown in the lower right corner. Cross-section intersections are shown with purple lines and are labelled accordingly.

<Insert Table S1> If table is large, upload as separate file but include caption in this document. Keep table captions in numerical order; it is acceptable to mix tables with captions and captions only (with files uploaded separately) in this document.

Supplemental Table Error! No text of specified style in document.**1.** Arrival information for the relocated hypocenters from SeaJade I and II. The arrivals are included in the file 'Supplemental_Table_A1.txt'. Hypocenter origin IDs are provided in the following format:

> \#, origin ID, station, travel-time(s), weight (1, by default), phase

> (repeat for each additional phase)

Supplemental Table Error! No text of specified style in document.**2.** Hypocenter information for the relocated events from SeaJade I and II. The locations are included in the file 'Supplemental_Table_A2.xlsx'. The columns are organized as follows:

> Origin ID, latitude, longitude, depth, X(m), Y(m), Z(m), EX(m), EY(m), EZ(m), year, month, day, hour, minute, second, magnitude, NCCP, NCCS, NCTP, NCTS, RCC(s), RCT(s), CID.

The X, Y, and Z parameters are measured in meters from the cluster centroid. EX, EY, and EZ are the estimated LSQR errors in E-W, N-S, and depth, respectively. NCCP, NCCS, NCTP, and NCTS, are the numbers of P and S phases used in the cross-correlation and travel-time difference datasets to locate the earthquakes, respectively. RCC and RCT are the time residuals, in seconds, for the cross-correlation and travel-time difference datasets, respectively.

Supplemental Table Error! No text of specified style in document.**3.** Focal mechanism information for events from SeaJade II.The focal mechanisms are included in the file 'Supplemental_Table_B1.xlsx'. Focal mechanisms from the Nootka Sequence have bolded italicized IDs. The columns are organized as follows:

> ID, Date, Latitude, Longitude, Depth, Magnitude, Strike, Dip, Rake, FP_unc, Aux_unc, num_P_pol, Wght % Misfit, Rank, Probability, num_SP, and Mode.

The depth parameter is measured in km. The magnitude parameter is measured in local magnitude (M_L). The parameters FP_unc and Aux_unc are the uncertainties for the primary and auxiliary fault planes, given in degrees. The parameter num_P_pol is the number of P first-motion polarities used in calculating the focal mechanism. Wght % Misfit is the weighted percent misfit of first motions. Rank can range from A to F (although only A-ranked data are provided), and is a measure of focal mechanism quality. Probability is a measure of how close the mechanism is to the true solution. num_SP is the number of S/P ratios used in calculating the focal mechanism. Mode is the failure mode of the focal mechanism; classification is derived from Alvarez-Gomez (2009): N – normal, R – reverse, S – strike-slip, N-S – normal oblique strike-slip, R-S – reverse oblique strike-slip, S-N – strike-slip oblique normal, S-R, strike-slip oblique reverse.

Supplemental Table Error! No text of specified style in document.**4.** P-wave tomography model from SeaJade II data. The model is included in the file 'Supplemental_Table_C1.txt', and the columns are organized as follows:

> Longitude, latitude, depth, V_P

Supplemental Table Error! No text of specified style in document.**5.** S-wave tomography model from SeaJade II data. The model is included in the file 'Supplemental_Table_C2.txt', and the columns are organized as follows:

Longitude, latitude, depth, V_s